CLIMATE CHANGE AND POTENTIAL HOTSPOTS OF COASTAL EROSION ALONG THE SOUTHERN CALIFORNIA COAST

A Paper From:
California Climate Change Center

Prepared By:
Peter N. Adams and Douglas L. Inman

DISCLAIMER

Arnold Schwarzenegger, *Governor*

FINAL PAPER

Acknowledgments

Preface

The California Energy Commission's Public Interest Energy Research (PIER) Program supports public interest energy research and development that will help improve the quality of life in California by bringing environmentally safe, affordable, and reliable energy services and products to the marketplace.

The PIER Program conducts public interest research, development, and demonstration (RD&D) projects to benefit California's electricity and natural gas ratepayers. The PIER Program strives to conduct the most promising public interest energy research by partnering with RD&D entities, including individuals, businesses, utilities, and public or private research institutions.

PIER funding efforts focus on the following RD&D program areas:

- Buildings End-Use Energy Efficiency
- Energy-Related Environmental Research
- Energy Systems Integration
- Environmentally Preferred Advanced Generation
- Industrial/Agricultural/Water End-Use Energy Efficiency
- Renewable Energy Technologies
- Transportation

In 2003, the California Energy Commission's PIER Program established the **California Climate Change Center** to document climate change research relevant to the state. This center is a virtual organization with core research activities at Scripps Institution of Oceanography and the University of California, Berkeley, complemented by efforts at other research institutions. Priority research areas defined in PIER's five-year Climate Change Research Plan are: monitoring, analysis, and modeling of climate; analysis of options to reduce greenhouse gas emissions; assessment of physical impacts and of adaptation strategies; and analysis of the economic consequences of both climate change impacts and the efforts designed to reduce emissions.

The California Climate Change Center Report Series details ongoing center-sponsored research. As interim project results, the information contained in these reports may change; authors should be contacted for the most recent project results. By providing ready access to this timely research, the center seeks to inform the public and expand dissemination of climate change information, thereby leveraging collaborative efforts and increasing the benefits of this research to California's citizens, environment, and economy.

For more information on the PIER Program, please visit the Energy Commission's website www.energy.ca.gov/pier/ or contract the Energy Commission at (916) 654-5164.

Table of Contents

List of Figures

List of Tables

Abstract

This paper presents a numerical model of the sedimentary and bedrock evolution of the Southern California coast. Inputs to the model include user-proscribed, deep-water (offshore) wave climate and seafloor bathymetry. By using a well-developed wave transformation routine (SWAN), the model calculates complete fields of wave height and direction over (1) a low-resolution (30 arc-second), coarse grid that includes the entire Southern California Bight, and (2) several high-resolution (3 arc-second), nested grids that cover contrasting coastlines within the bight. Through numerical experiments, the model was exercised to illustrate its potential to explore impacts of climate change on decadal scale coastal evolution over select regions. At the Santa Barbara site, the first experiment investigated the effects of changes in deep-water wave direction on magnitudes and locations of erosional hotspots. Notably, our results show that a sheltered portion of coast can change its character from accretional to erosional in response to an increased deep-water wave period, and this effect is enhanced as the deep-water wave direction becomes more westerly, as opposed to north-westerly. Increased wave periods and more westerly directions associated with El Niño wave events might therefore exacerbate the erosional response at sites where wide sandy beaches persisted for many years prior to the increased frequency of El Niño events. The second experiment, conducted for the beaches of Los Angeles County and Orange County, modeled the persistence of naturally occurring erosional hotspots for a recent hindcast wave climate that includes variability in the Pacific Decadal Oscillation and the El Niño Southern Oscillation. Although the different beaches of the Santa Monica Bay exhibit various chronic behavior (from erosional to accretional), the spatial patterns of erosion and accretion associated with the El Niño winter of 1982–1983 were consistently more severe than ordinarily observed. Lastly, we present a methodology for calculating the effect of sea level rise on sea cliff retreat based on nearshore bedrock platform slope and simple geometric considerations. We apply this technique to a relatively stable portion of the Southern California coast—the Torrey Pines littoral subcell—and provide the estimate that a 1 meter rise in sea level could drive a sea cliff retreat of approximately 50 meters landward.

Keywords: Coastal erosion, wave climate, Southern California, sea level rise, numerical modeling

1.0 Introduction

Climate change poses a significant challenge to the future of California's coast. Nearly 80% of the population of the state of California inhabits the narrow swath of land within 30 miles of the coast (Griggs et al. 2005). Attendant with this population distribution is the infrastructure necessary to support society, including interstate highways, electrical power generation plants, and various commerce facilities. Given the overwhelming evidence that global climate change is upon us and the recognition that eustatic sea level rise is a fundamental result of climate change, it is imperative to assess the oceanographic and geomorphic changes expected within the coastal zone, to mitigate the effects of climate change on coastal communities. Effective planning for the future of the California coast will need to draw on climate models that predict the forcing scenarios and coastal change models that predict the coast's response.

Evaluating the causes and consequences of coastal change requires an understanding of the processes involved in coastal evolution. Waves, currents, and sediment supply are the primary controls on coastal evolution; any changes in global climate which alter the timing and magnitude of storms and/or raise global sea level will have severe consequences for beaches, coastlines, and coastal structures.

We may organize the effects of climate change on the California coastal zone into the four main categories:

1. Sea level rise and the associated landward migration of the shoreline (inundation), along the cliffed and the sandy beach portions of the coast.

2. Potential changes in littoral sediment budgets caused by a redistribution of nearshore wave energy resulting from sea level rise alone.

3. Potential changes in littoral sediment budgets caused by changes in deep-water storm patterns and intensity, resulting from warming of the ocean-atmosphere system (the main focus of this paper).

4. Potential changes to sediment supply to the littoral system from river discharge.

In this paper, we present a detailed numerical model, which calculates the locations and magnitudes of hotspots of coastal erosion as a function of changes in deep water wave fields that might accompany climate change. We then use the model to conduct a series of numerical experiments to illustrate the model's utility in addressing questions of climate change and coastal evolution. The numerical experiments chosen address the following questions:

1. How do changes in deep water wave direction, a likely result of climate change, affect the pattern of erosional hotspot distribution along exposed and sheltered portions of the Southern California Bight? (Section 3.1)

2. What is the variability of potential divergence of longshore drift over a complete cycle of the Pacific Decadal Oscillation, including the effects of severe El Niño winter storms? (Section 3.2)

3. How will a 1-meter rise in eustatic sea level translate into sea cliff retreat at a relatively stable reach of the Southern California Bight? (Section 3.3)

The purpose of this paper is to present a numerical model and framework for exploring the effects of climate change on the Southern California coast, and to illustrate the utility of such a model through the aforementioned numerical experiments. We specifically chose different sites for each of the first two groups of calculations to show that the model was robust over a range of coastal orientations.

1.1. Background on Coastal Evolution Modeling

For many years, numerical models of coastal sedimentary processes were developed only by engineers, in studies that targeted coastal structure emplacement and the subsequent effects on cross-shore beach profiles and longshore patterns of sediment transport. With applications aimed at aiding shipping industry, these models focused on "real-time" processes with time-windows that covered seasonal to annual scales at most (Larson and Kraus 1989).

In the past 20 years, tremendous strides have been made in the field of geomorphic evolution modeling in response to long-term climate variation. Examples from such varied environments as alpine glacial valleys (MacGregor et al. 2000), terraced fluvial plains (Hancock and Anderson 2002), and tectonically active coasts (Anderson et al. 1999) provide hope that we can combine the physical processes of terrestrial sedimentary sources (rivers and sea cliffs) with nearshore oceanographic processes (waves, tides, and currents) to develop an understanding of how sedimentary coasts respond to climatic changes. Within the scope of this study, we focus on relatively short-term geomorphic changes that may occur on the decadal to century time scale.

Most recently, researchers have worked to develop so-called "one-line" numerical models of coastal evolution, in which the assumption is made that cross-shore profile shape is constant, while shoreline position varies (Pelnard-Considere 1956). Conservation of mass is the fundamental concept employed in one-line models, wherein sediment accumulation (or depletion) within a coastal compartment results from the divergence of littoral drift (i.e., the first spatial derivative of volumetric longshore sediment transport rate). Utilizing a one-line coastal evolution model, Ashton et al. (2001) explored the concept of high-angle waves in the stability of large, coastal planform features. In a recent study by Ruggiero et al. (2006), a one-line coastal evolution model (UNIBEST) was used in conjunction with a wave transformation model (SWAN) to investigate probabilities of decadal shoreline change along the Washington coast. List et al. (2007) have explored predictions of longshore sediment transport gradients with the advanced, process-based Delft3d nearshore flow model.

1.2. Regional Setting: Southern California Bight

For the purposes of this study, we consider the Southern California Bight to extend from a northwestern-most boundary at Point Arguello (34.58°, -120.65°, Figure 1-1) to the U.S.-Mexico border (32.54°, -117.12°, Figure 1-1) south of San Diego. Within this region, we have also established several subregions (~10 kilometers [km] to ~100 km reaches) where coastal evolution can be modeled and studied with higher spatial resolution (Figure 1-2). Throughout this paper, we refer to these subregions as "nests," a term borrowed from the terminology of the wave transformation model, covered in greater detail in Section 2.3. In sections 1.2.1 thru 1.2.5, we describe the geologic setting, sedimentary sources, littoral cells, regional wave climate, and sea level rise history for the Southern California Bight.
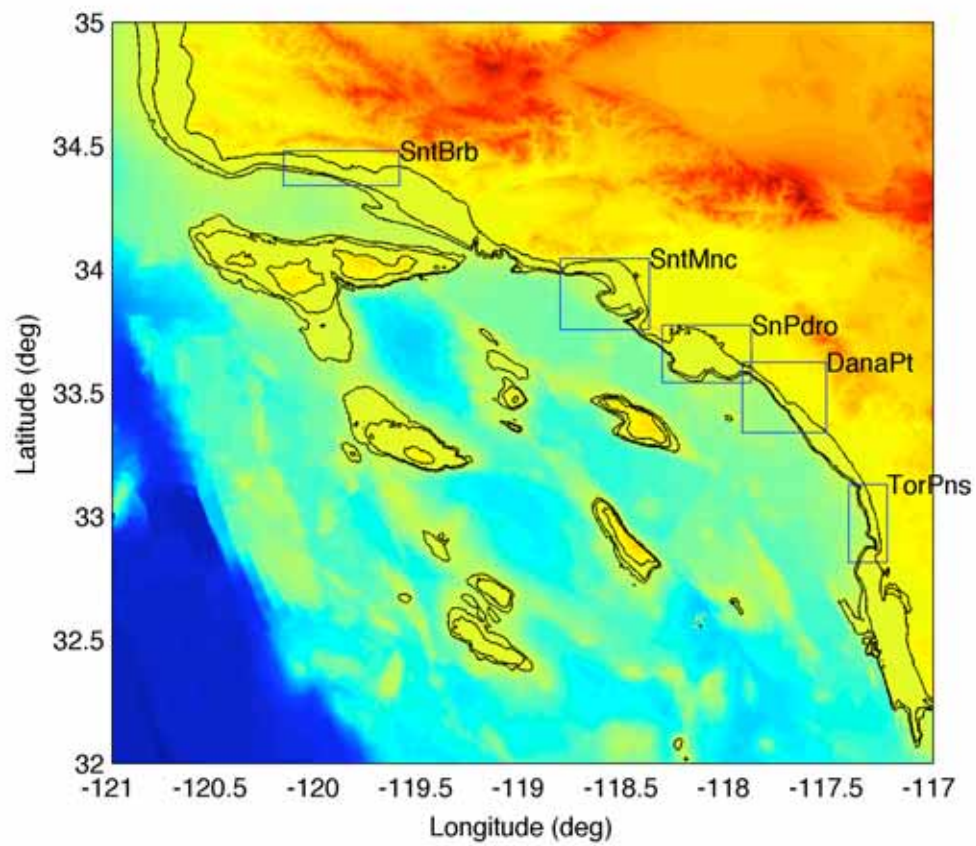
Figure 1-1. Map of the Southern California Bight showing the five nested regions used in this study for detailed modeling analysis

Nest ID = n03,
Nest Name = SntBrb

Nest ID = n06,
Nest Name = SntMnc
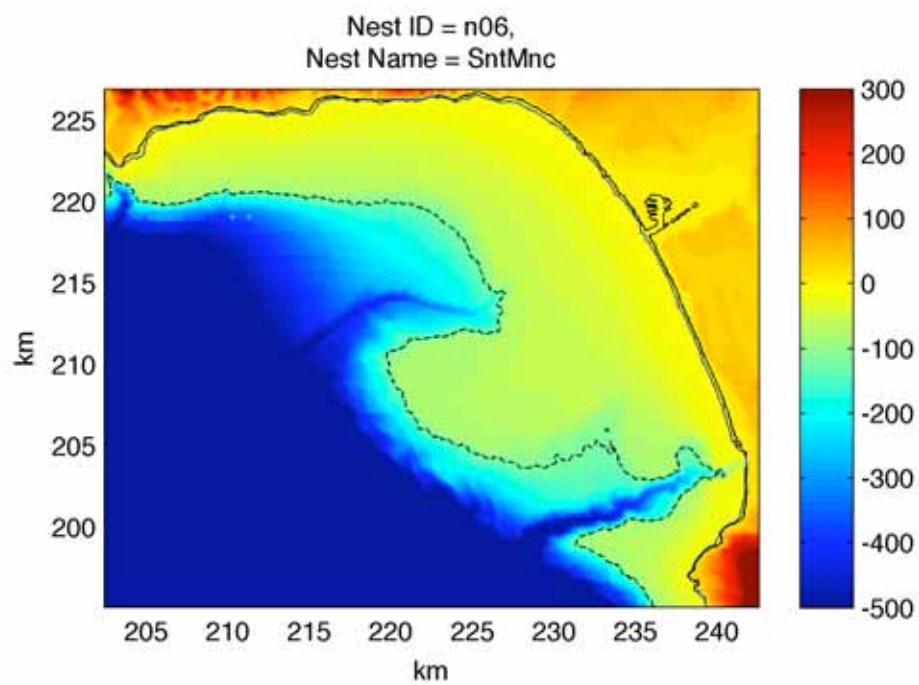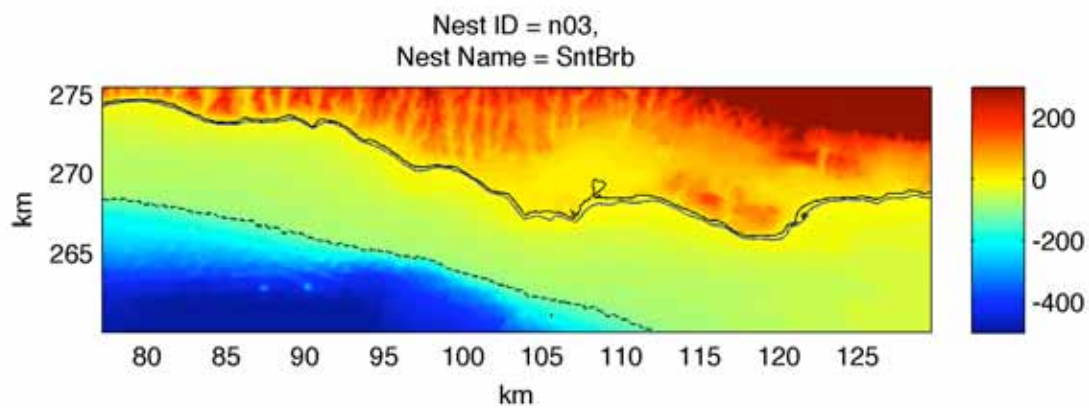
Nest ID = n08,
Nest Name = SnPdro
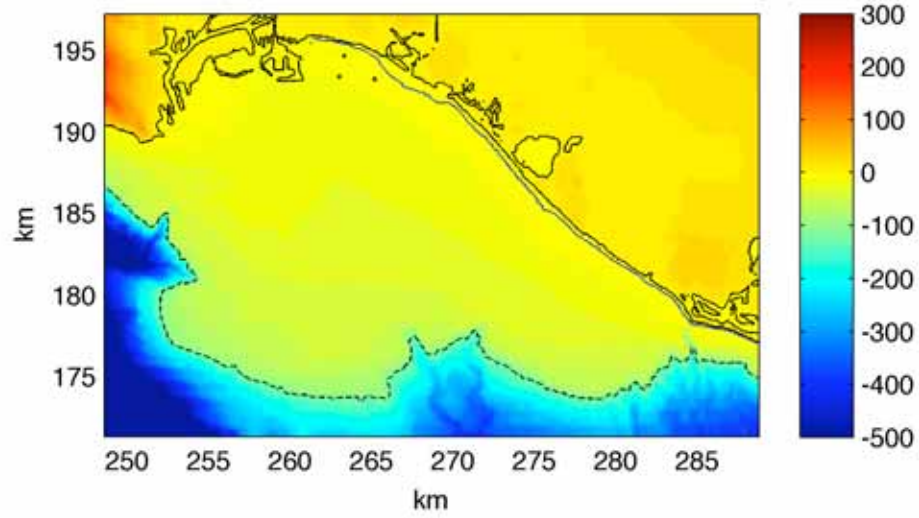
Nest ID = n09,
Nest Name = DanaPt
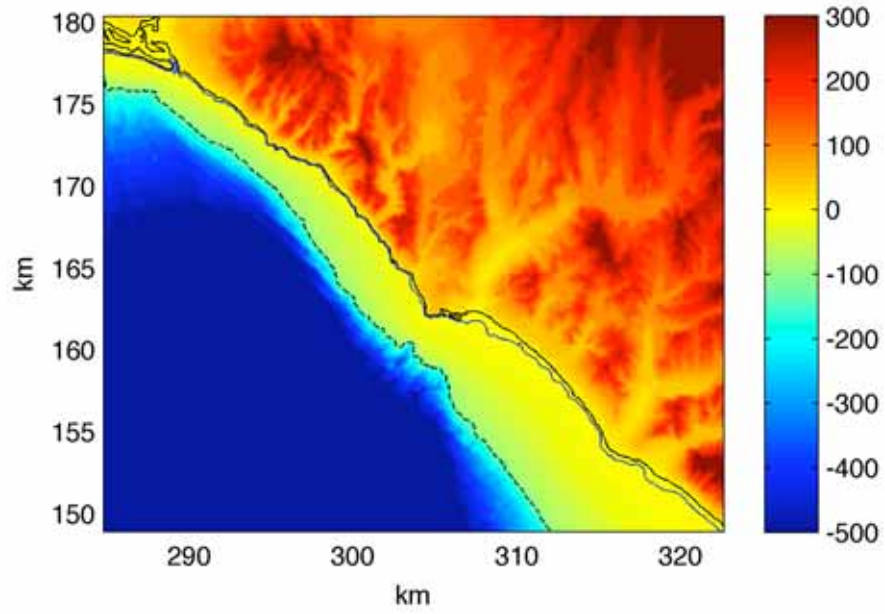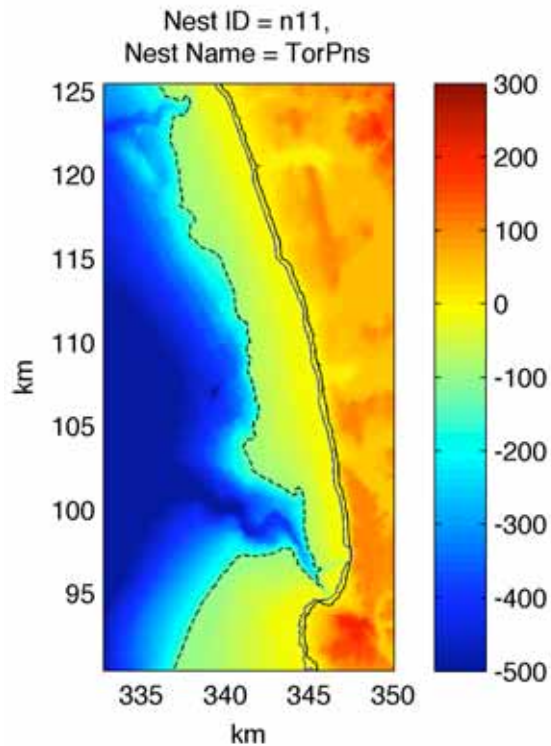
Figure 1-2. Bathymetry of five detailed nested regions used in this study. Nests are referred to as Santa Barbara (SntBrb), Santa Monica Bay (SntMnc), San Pedro (SnPdro), Dana Point (DanaPt), and Torrey Pines (TorPns), respectively. In each nest view, the solid black line shows modern, mean sea level shoreline, the solid blue line shows the location of the 5-meter isobath, and the dashed black line shows the location of the 120-meter isobath, considered to be the edge of the continental shelf. Color bars correspond bathymetric elevation in meters above/below mean sea level.

1.2.1. Geologic Setting

Tectonic processes are responsible for shaping the shallow ocean basins, continental shelf, and large-scale terrestrial landmasses adjacent to Southern California's coast. The tectonic setting for Southern California is considered to be a collisional or active margin, which occurs where two plates impinge upon one another (Inman and Nordstrom 1971). On the active transform boundary between the Pacific and North American plates, the leading edge of the plate boundaries have been folded and fractured by transpressional plate motions. In particular, the coastal mountain ranges and local shelf basins have been constructed by crustal displacement and tectonic activity along a network of subparallel strike-slip faults which characterize the North American plate-Pacific plate interface (Hogarth et al. 2007). In general, these motions have resulted in the highly irregular, complex bathymetry that makes up the California Borderlands(Legg 1991; Shepard and Emery 1941), decorated with the subaerially exposed Channel Islands, as well as numerous submerged seamounts and troughs, shown in Figure 1-3. This collisional margin coast is typified by a narrow, steep continental shelf (~10 km wide),

6

deeply incised submarine canyons, and beaches backed by resistant, bedrock sea cliffs. This coastal geomorphology contrasts with the passive or trailing edge margin of the eastern United States, where sedimentary processes dominate, resulting in a broad subaerial coastal plain and a continental shelf that is wide (~50 km to 100 km) and gently sloping.
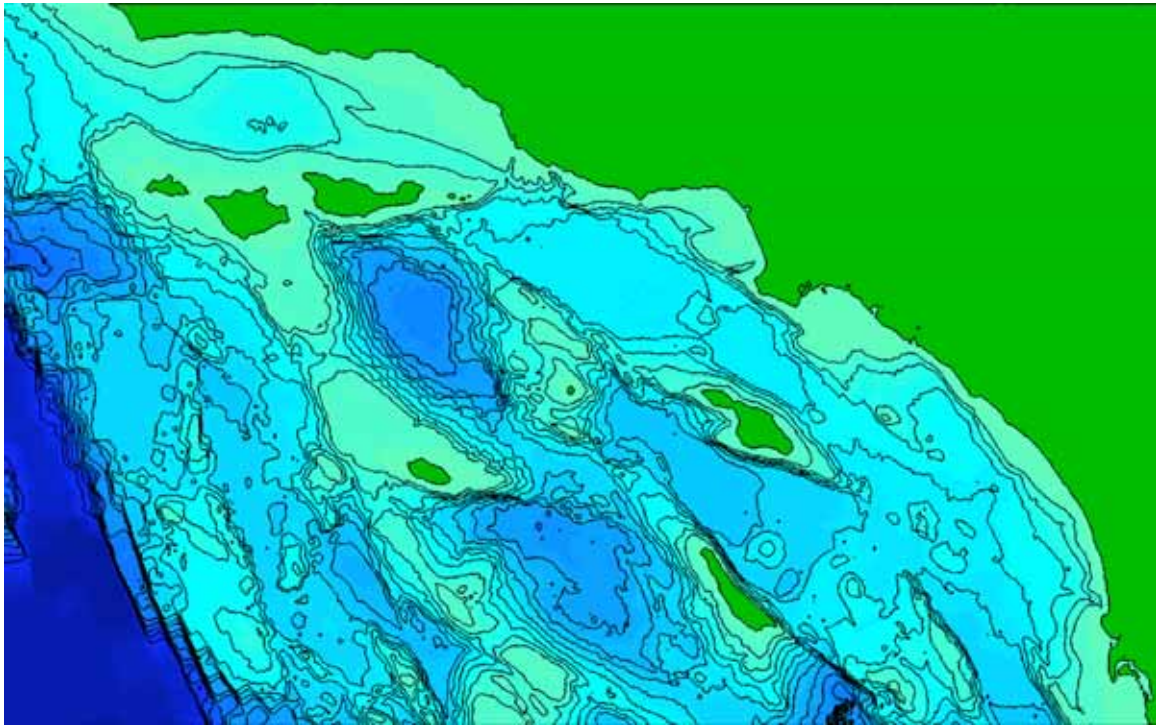
Figure 1-3. Complex bathymetry of the Southern California Bight. The depth contour interval is 200 meters.

1.2.2. Sedimentary Sources

Globally, the sources of sediment to the coastal zone are dominantly fluvial. Where rivers meet the coast in Southern California, there are often local depositional basins (sedimentary deltas), which temporarily store fluvial sediment as it awaits incorporation into longshore sediment in the littoral system. The major rivers responsible for delivering sediment to the Southern California coast are the Santa Maria, the Santa Ynez, the Santa Clara, the Los Angeles, the San Gabriel, the Santa Ana River, the Santa Margarita, the San Luis Rey, and the Tijuana. Each of the aforementioned rivers drain catchments that exceed 1000 square kilometers (km^2) in area (Inman and Jenkins 1999). Intermittent streams follow steep-sided canyons as they emerge from the coastal ranges, and all but a few drainages are relatively small with high gradients. It has been shown that rivers draining small, mountainous, coastal catchments provide a surprisingly large fraction of littoral sediment to the nearshore zone (Milliman 1995; Milliman and Syvitski 1992), and that sediment discharge from these rivers can be significantly influenced by climatic variability (Cayan et al. 1999; Farnsworth and Milliman 2003; Warrick and Milliman 2003). With

Southern California's semiarid climate, sediment supply to the coast is limited to runoff events from winter storms, making the beaches sand limited.

1.2.3. Littoral Cells

The littoral cell, shown schematically in Figure 1-4, is the coastal compartment that contains the sources, transport paths, and sinks of sediment (Inman 2005; Inman and Frautschy 1965). Sediment sources on cliffed coasts are (1) rivers, which deliver the products of terrestrial erosion, and (2) sea cliffs, which erode and retreat due to attack by waves. Fine suspended sediment is carried offshore in turbid plumes and deposited in deeper water (e.g., Warrick and Milliman 2003), whereas sand is transported along the shore by waves and wave-generated currents to maintain beaches. Transport rates along open ocean coasts range from 150,000 to 600,000 cubic meters per year (m^3/yr). A sediment sink is considered to be the terminus of a littoral cell, and it usually consists of a submarine canyon (Figure 1-4). Along California's tectonically active coast, rocky headlands often form the boundaries of littoral cells, as longshore sediment transport is often blocked there (Figure 1-5). For example, Oceanside littoral cell begins at the rocky headland of Dana Point, whereas the San Pedro cell to the north ends at Newport Submarine Canyon (Figure 1-2, Dana Point). The coastline between these major cells consists of a series of pocket beaches between headlands, known as the Crystal Cove Subcells. This tells the modeler that sand transport is limited to individual pocket beaches of the subcells and does not begin again as littoral drift until well south of Dana Point. Accordingly, the entrance channel to Dana Point Harbor just south of Dana Point traps negligible amounts of sand; whereas Oceanside Harbor at the midpoint of the Oceanside cell requires constant dredging. The littoral cell and its associated budget of sediment are useful as a tool to organize coastal compartments and are valuable for regional coastal management.
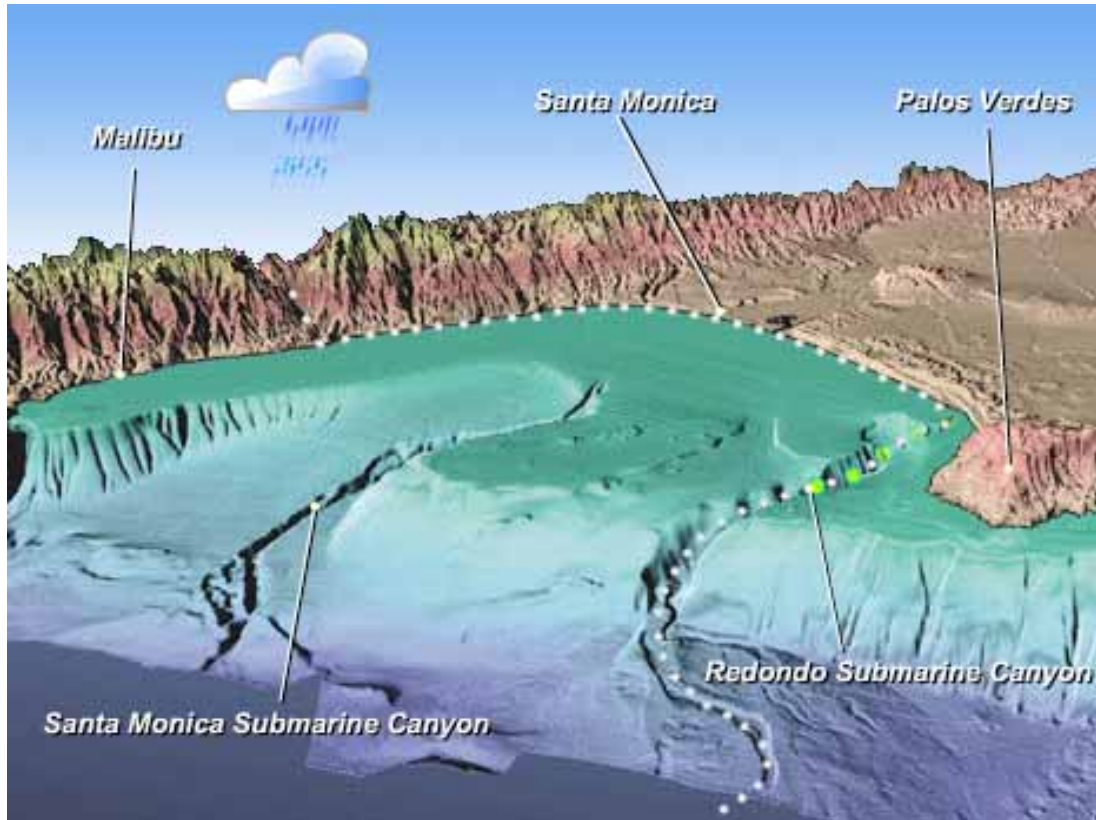
Figure 1-4. Oblique view of Santa Monica Bay bathymetry showing paths of littoral transport within a littoral cell. Redondo submarine canyon is a local sink for littoral sediment.

Image courtesy of the Coastal Morphology Group, Scripps Institution of Oceanography, University of California.

1.2.4. Regional Wave Climate

The wave climate of Southern California has been extensively studied since the early oceanographic investigations of the 1940s to support the military effort during World War II. Sverdrup and Munk (1947) applied the theoretical relationships of wave transformation to predict breakers and surf along the beaches of La Jolla, California. During the 1980s the National Oceanic and Atmospheric Administration (NOAA) began deploying wave buoys to monitor conditions within the Southern California Bight (SCB). This effort has been improved by the development of the Coastal Data Information Page (CDIP) program, which was started at Scripps Institution of Oceanography by Dr. Richard Seymour in 1975.

The presence of the Channel Islands (Figures 1-1 and 1-3) significantly alters the deep-water (open ocean) wave climate to a more complicated nearshore wave field along the Southern California coast. The islands intercept waves approaching from almost any direction and the shallow water bathymetry adjacent to the islands refracts and reorients wave rays to produce a complicated wave energy distribution along the coast of the Southern California mainland. Several studies have targeted the sheltering effect of the Channel Islands within the SCB and the complexity of modeling wave transformation through such a complicated bathymetry (e.g., O'Reilly 1993; O'Reilly and Guza 1993; Pawka 1983; Rogers et al. 2007). The resulting distribution of wave energy at the coast consists of dramatic longshore variability in wave

energy flux and radiation stress. These factors are considered to be fundamental in generating the nearshore currents responsible for longshore sediment transport and the maintenance of sandy beaches.

Recently, Adams et al. (2008) examined a 50-year (1948–1998) numerical hindcast of deep-water, winter wave heights, periods, and directions for location 33°N/121.5°W, to understand the correlation of decadal-to-interannual climate variability with offshore wave fields. Their study found that El Niño-type winters during Pacific Decadal Oscillation (PDO) warm phase have significantly more energetic wave fields than those during PDO-cool phase, suggesting an interesting connection between global climate change and coastal evolution, based on patterns of storminess (Figure 1-6).

Figure 1-5. Distribution of littoral cells within the Southern California Bight

Image courtesy of the Coastal Morphology Group, Scripps Institution of Oceanography, University of California (http://coastalchange.ucsd.edu/st3_basics/littoralcell.html).
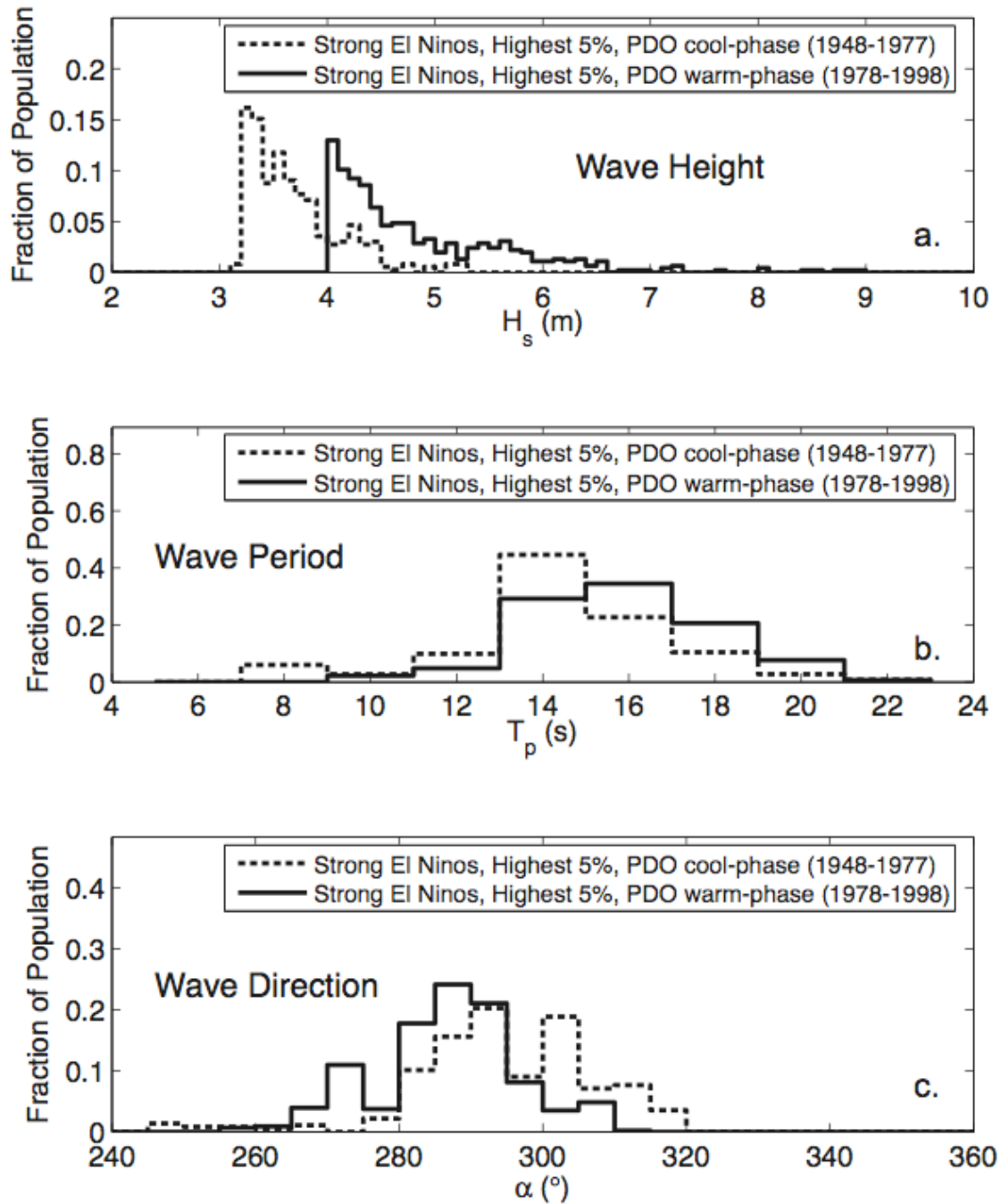
Figure 1-6. Population distributions of wave height, period, and direction for the National Center for Atmospheric Research-National Centers for Environmental Prediction (NCAR-NCEP) numerical hindcast of deep-water winter wave climates (1948–1998) for location 33˚N/121.5˚W. Analysis targets variability in El Niño winter wave characteristics commensurate with changes in Pacific Decadal Oscillation phase.

1.2.5. Sea Level History and Projections

During the Quaternary geologic period, eustatic (global) sea level has experienced wide-ranging fluctuation due in large part to climatic variability (Ruddiman 2002). Since the last glacial maximum (LGM) approximately 18–20 thousand years ago, sea level has been rising from approximately 120 meters below modern level to its present state (Figure 1-7). The details of this transgression indicate that the rate of sea level rise has not been steady. Exceptionally warm periods drive increased rates of melting of glacial ice, which provide a pulse of water to the world's oceans, causing short-lived intervals of rapid sea level rise. Over the last five thousand years, eustatic sea level has been relatively stable or rising very slowly, save for the recent increase in sea level rise rate, estimated from tide gauge records from San Francisco, to a value of 2.2 millimeters [mm] per year (20 centimeters [cm] per century) over the last several decades (Flick et al. 2003). From a set of climate simulations for a series of different greenhouse gas emissions scenarios, Cayan et al. (2008) calculate a potential sea level rise of up to 72 cm by 2070–2099 (7.9 to 11.6 mm/yr). This estimate indicates a 3.6x to 5.3x increase in sea level rise rate. This current estimate illustrates the need to understand the potential hazards threatening the California coast due to inundation by sea level rise and changes in wave storminess due to sea level rise–induced changes in climatic circulation.
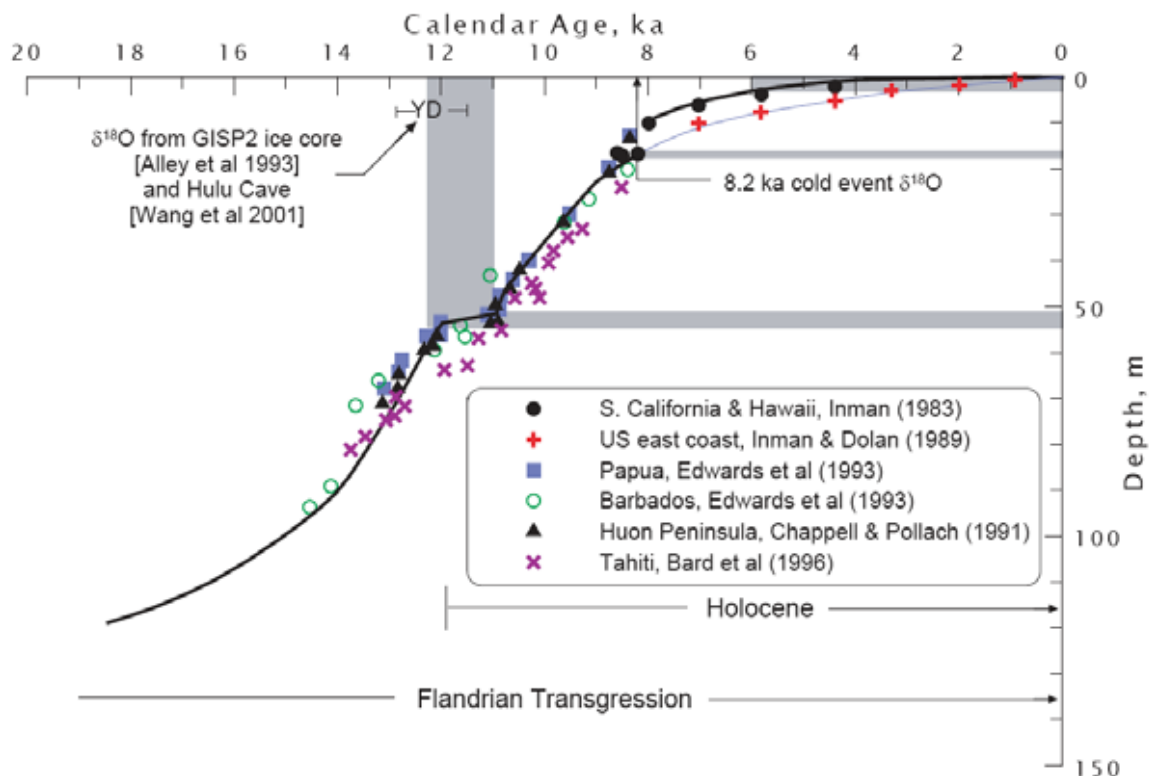
Figure 1-7. Sea level history since the last glacial maximum (~18–20 kiloannum), compiled from numerous studies worldwide

Image courtesy of coastal Morphology Group, Scripps Institution of Oceanography, University of California. (Previously published in Inman et al. 2005b.)

2.0 Methods

In this project, the primary method to study potential coastal evolution in Southern California resulting from climate change is numerical modeling. Models of natural systems are valuable to geomorphologists and engineers through two techniques: (1) if the processes governing the system are definable by mathematical relationships, a numerical model can be used as a predictive tool to identify likely behavior of the system under proscribed conditions, and (2) if the interactions among interrelated geomorphic processes are well-understood, numerical models can be used to explore parameter space through experiments to better quantify how changes in an independent variable (e.g., wave direction) can influence the behavior of a dependent variable (e.g., coastal erosion/accretion.)

To provide insight on how climate change might affect the Southern California coast within the next century, we utilized both of the aforementioned techniques. First, we conducted a series of controlled numerical experiments to examine the effects of wave direction on the magnitude and location of hotspots of coastal erosion within a 10-km reach of the Santa Barbara coast (the Goleta subcell). Second, we calculated annual (winter) values for the spatial distribution of potential divergence of longshore drift along the coasts of Los Angeles County (between Point Dume and Palos Verdes Point, ~ 70 km), for the deep-water wave climate hindcast of the years 1948–1998. Third and lastly, we used geometrical considerations and a conservative estimate of sea level rise for the next century to show how sea cliffs along a relatively stable coastline may respond to climate change. This last calculation represents conditions likely from a rough, yet conservative, estimate of one effect of global climate change on volumetric increase in water storage in the Earth's oceans.

What follows in this section (2.1–2.5) is an overview presentation of the model architecture and detailed descriptions of model components. In subsection 2.1, we begin the description of methodology by showing a diagram that illustrates how model components interact. Then, in subsection 2.2, we review the basic inputs and outputs of the model, and provide some resources for obtaining critical bathymetric and wave climate inputs. In subsection 2.3, we explain how the complicated, spectral wave transformation portion of the modeling (SWAN) is conducted and simplified by using an output lookup table to establish wider model applicability. In subsection 2.4, we cover the detailed modules of the longshore sediment transport modeling, herein named the Coastal Geomorphic Evolution Model (CGEM), which provides the essence of sedimentary coastal evolution modeling on the spatial scale targeted in this study (10s to 100s of kilometers of coastline). Lastly, in subsection 2.5, we highlight the cautionary limitations of the coastal evolution model and comment on the range of applicability for proper model use.

2.1. Model Overview and General Architecture

The numerical model used to simulate coastal evolution in this study is generally organized into two major components: (1) SWAN, a freely available FORTRAN program, developed by the Delft Hydraulics Group (Booij et al. 1999), and (2) CGEM, a series of MATLAB codes developed for this project. These two components compute the wave transformations and longshore sediment transport calculations, respectively, and interact by passing SWAN calculations to CGEM, as shown schematically in Figure 2-1. By proscribing a deep-water wave field (consisting of wave heights, periods, and directions) and digital bathymetry (topography

13

of the ocean floor), SWAN calculates the patterns of refraction, diffraction, and redistribution of wave energy as waves move from the open ocean across the complicated bathymetry of the Southern California Bight (Figure 1-3) to the nearshore locations demarcated by the map-view location of the 5-meter isobath (bathymetric contour). At the location of the 5-meter isobath, CGEM uses the information on nearshore wave conditions, computed by SWAN, to calculate angle of incidence, longshore component of wave energy flux, and longshore sediment transport potential (assuming a transport-limited scenario) along the entire reach of the portion of coast being analyzed. Detailed explanations of each component and the individual modules of CGEM are discussed in subsection 2.4.
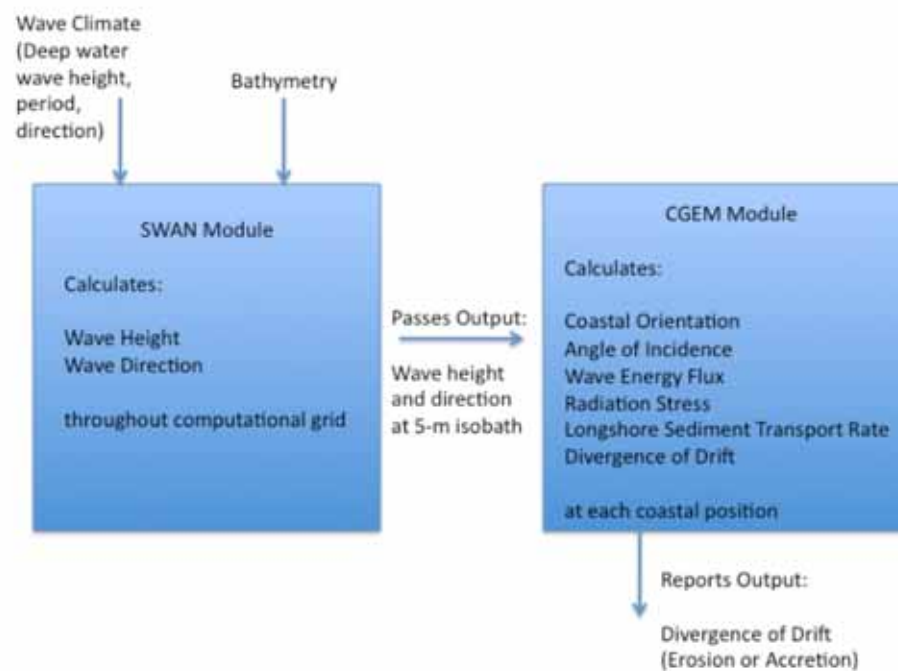
Figure 2-1. Coastal Evolution Model architecture showing the relationship of the SWAN and CGEM modules

2.2.   Model Inputs

The coastal evolution model, which consists of the wave transformation portion (SWAN) and the longshore sediment transport portion (CGEM), requires only two general inputs: bathymetry and offshore (deep-water) wave conditions. In subsections 2.2.1 and 2.2.2, we describe the details, requirements, and formats of these two general inputs.

2.2.1. Bathymetric Data

Ocean bathymetry (i.e., underwater topography) exhibits a strong control on the direction and rate of wave energy translation. Linear Airy wave theory, used when wave height is much

smaller than wavelength and water depth, predicts that wave orbital motions interact to a depth of approximately half the wavelength (Komar 1998). When the water depth is shallower than half the wavelength, interaction of wave orbitals with the sea floor causes shoaling transformation and refraction of waves. Therefore, the spatial pattern of nearshore wave energy depends strongly on the distribution of seafloor elevation.

Bathymetric data are required for SWAN model simulations of wave transformation. Although, SWAN can accept bathymetric data in many formats, we chose to use a grid of bathymetry of the Southern California Bight sea floor with a spatial resolution of 3 arc-seconds (~93 meters latitudinal spacing, ~77 meters longitudinal spacing), ranging from 32˚ to 35˚ north latitude and -121˚ to -117˚ longitude (3600 by 4800 = 1.728e6 grid cells).

Bathymetric data used in this study were obtained from the National Geophysical Data Center (NGDC–NOAA) 3 arc-second U.S. coastal relief model grid database.[1] This database provides coverage of nearshore, shelf, and proximal deep ocean bathymetry for the coterminous U.S. coastline, including Hawaii and Puerto Rico.

By using a grid-based bathymetry, changing sea level is a trivial matter performed simply by adding a scalar value to each element of water depths in the bathymetric matrix. This is further simplified by the seamless coverage of the database from offshore to onshore terrain.

2.2.2. Offshore Wave Climate

To proscribe wave climate for the SWAN module, information on wave height, period, and direction for the wave field must be provided. For wave height, some representation of the central tendency must be provided; in all of our simulations, we provide significant wave height, which is defined as the average of the height of the largest one-third of the waves as measured over a specific time interval. For wave period, we provide a spectrally dominant, "peak" period and assume a Joint North Sea Wave Project (JONSWAP) distribution of frequency for the remainder of the spectrum (Hasselmann et al. 1973). For the wave direction, we provide a spectrally dominant wave direction and a "spread angle" whose cosine is calculated to account for the remainder of energy distribution within the directional spectrum.

To provide an instantaneous snapshot of the wave field in the region, a stationary SWAN run is conducted using the three specific wave climate variables, as described above. The output result is the complete stationary wave field (values of height and direction) at each grid point within the model domain. According to Airy wave theory, the wave period is not expected to change, but values may differ from the mean, dominant period, as the JONSWAP distribution is used as an input.

The wave data set used in this study comes from the numerical hindcast for the 50-year period 1948–1998 described in Graham and Diaz (2001) and Graham (2003). The wind forcing for the wave data comes from the NCEP-NCAR reanalysis project (Kalnay et al. 1996; Kistler et al. 2001). This data set represents the last full cycle of decadal climate change (full PDO cycle). The hindcast domain is the North Pacific Ocean (20˚N–60˚N, 150˚W–110˚W) with a spatial resolution of 1˚ latitude x 1.5˚ longitude. Data were produced for winter months (DJFM), with 3 hourly spectra recorded in 20 frequency bins (covering the wave period range of ~ 4.5 s–26 s), and 5

---

[1] See www.ngdc.noaa.gov/mgg/coastal/coastal.html.

degree directional resolution grouped in 72 bins. The summary outputs used in this study, calculated from wave energy in the spectral bins, are (1) significant wave height (Hs) in deep water, (2) peak (spectrally dominant) wave period of the significant wave height (Ts), and (3) peak (spectrally dominant) wave direction (α), for the reference deep-water location 33˚N, 121.5˚W; a hindcast node in the model domain. This location was chosen for its position west (oceanward) of the Channel Islands in the SCB. This location has the advantage of representing an open ocean wave climate signal, not subject to island sheltering, shoaling, and the complex refraction and diffraction patterns within the SCB, discussed by Pawka (1983), Pawka et al. (1984), and O'Reilly and Guza (1993).

For current wave time series data available for numerous sites along the U.S. coast, the reader is referred to the NOAA National Buoy Data Center (NDBC) website:

www.ndbc.noaa.gov/

and the Coastal Data Information Page (CDIP):

http://cdip.ucsd.edu/.

2.3. Wave Transformation Modeling

The wave transformation modeling was conducted on a 3-node (6 processor) Linux cluster at the University of Florida Geomorphology Lab, where we were able to take advantage of parallel processing computations. As an example to demonstrate the advantage of parallel processing for the wave transformation modeling, we provide the following comparison. A typical SWAN run for the entire Southern California Bight including separate runs for three nested subsections is executed in approximately 21 minutes on an Apple Mac Pro (2.8 GHz, Quad-Core Intel Xeon Processor) in single processor mode. The same simulation requires only 3 minutes to complete on our Linux cluster, resulting in a ~700% increase in computational efficiency.

Although SWAN is written in FORTRAN, as part of this project we have written a series of MATLAB .m-files to write the required input files for SWAN (.swn files) and execute both the main grid and nested grid calculations of wave transformation.

By "main grid" calculations, we refer to the coarsely spaced (30 arc-second) initial pass SWAN computation (in stationary mode), which solves for the complete 4˚ x 3˚ grid field of wave conditions over the entire Southern California Bight. This results in a 480 x 360 matrix of wave heights, periods, and directions, wherein each value represents the conditions for a ~0.75 km^2 area of sea-surface. Once the main grid (coarse) wave conditions have been computed, these values are used as boundary conditions at the oceanic edges of the nested grid locations. The relationship of grid sizes and spacing for main grid and nests are shown in Figure 2-2.
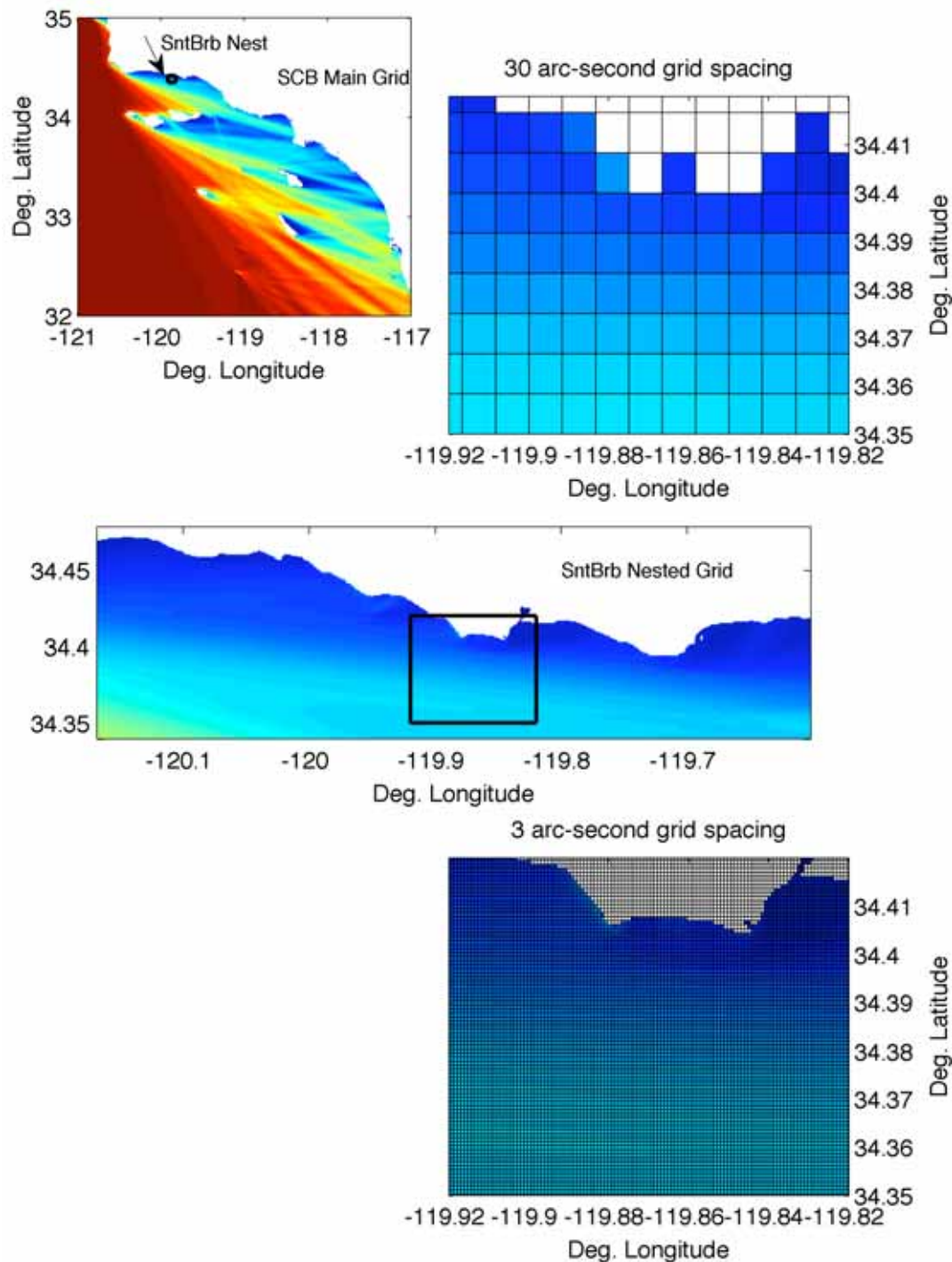
Figure 2-2. Illustration of grid spacing used for "main grid" (30 arc-second spacing) and "nested grids" (3 arc-second spacing) in SWAN modeling of wave transformation

2.3.1. Lookup Table Development

We reasoned that the most effective way to simulate long time series of wave transformation within the Southern California Bight was to develop a three-dimensional lookup table of deep-

17

water conditions for wave height, wave period, and wave direction. This method was introduced by Ruggiero et al. (2006) and proved to be an efficient technique for simulating long-term shoreline change. By doing so, any triplet of wave conditions could be approximated by the closest values for which a SWAN simulation had already been conducted. For example, if the deep water wave conditions were: Hs= 2.1 m, Tp=12.7s, and Dd=292˚, the closest triplet of conditions would be Hs=2.0m, Tp=13.0s, and Dd=290˚. This technique significantly speeds analyses, as each triplet of wave conditions can be "looked-up" to its nearest proxy triplet—an operation that takes a fraction of a second of computer execution time, as opposed to re-running SWAN for the specific set of conditions, which would take approximately 2–3 minutes of computation time (or ~21 minutes when not employing parallel processing.)

We define the interval spacing for the three offshore wave climate variables in the lookup table by examining the joint distributions of the three offshore wave climate variables from the numerical hindcast for the 50-year period 1948–1998 described in Graham and Diaz (2001) and Graham (2003), described in Section 2.2.2, above. These joint distributions are shown in Figures 2-3, 2-4, and 2-5. The complete set of SWAN runs for the lookup tables, at two separate sea level conditions—(a) modern day sea level, and (b) + 1 meter above modern day sea level—are illustrated graphically in Figures 2-6 and 2-7. These figures show the unique deep-water wave input conditions (Hs, Tp, and Dd) used for each SWAN run, whose numbers are identified on the horizontal axis. Over a three-month period (May–July, 2008) 7,392 SWAN main grid runs and 36,960 nested grid runs were executed to generate these lookup tables, whose permutations span the following range of conditions:

- Deep-water significant wave height (Hs) varies from 0.5 to 5.5 m, with an interval spacing of 0.5 m (11 conditions).
- Deep-water peak wave period (Tp) varies from 9 to 20 seconds, with an interval spacing of 1 s (12 conditions).
- Deep-water dominant wave direction (Dd) varies from 220 to 355 degrees, with an interval spacing of 5 degrees (28 conditions).
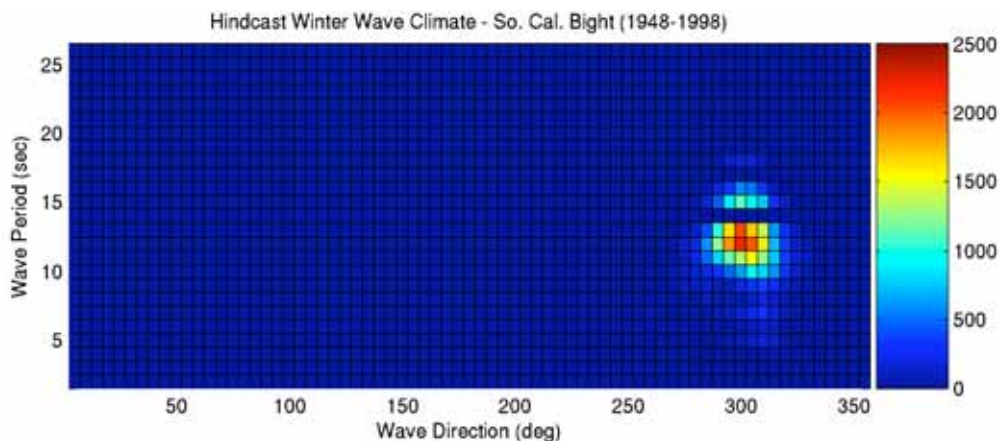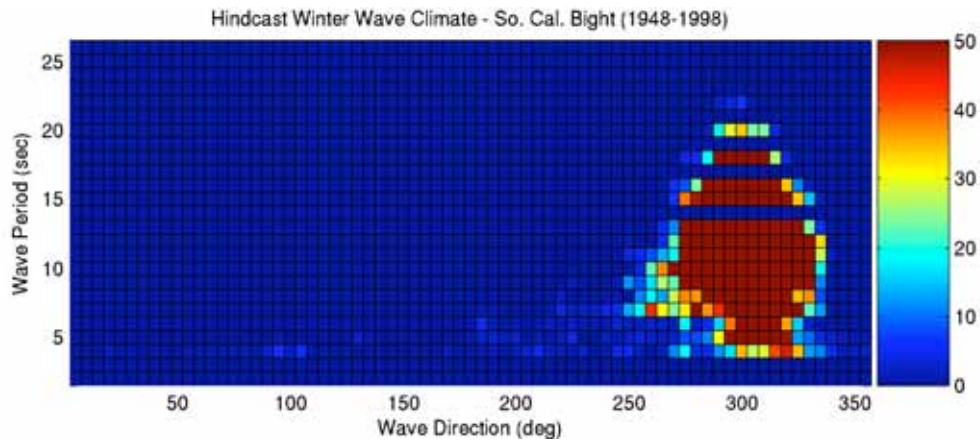
Figure 2-3. Joint distributions wave period and wave direction for the NCAR-NCEP numerical hindcast of deep-water winter wave climates (1948–1998) for location 33˚N/121.5˚W. The color map differs for each diagram to better show the spread of data distribution. Units for the color bar are counts (number of 3-hourly observations).
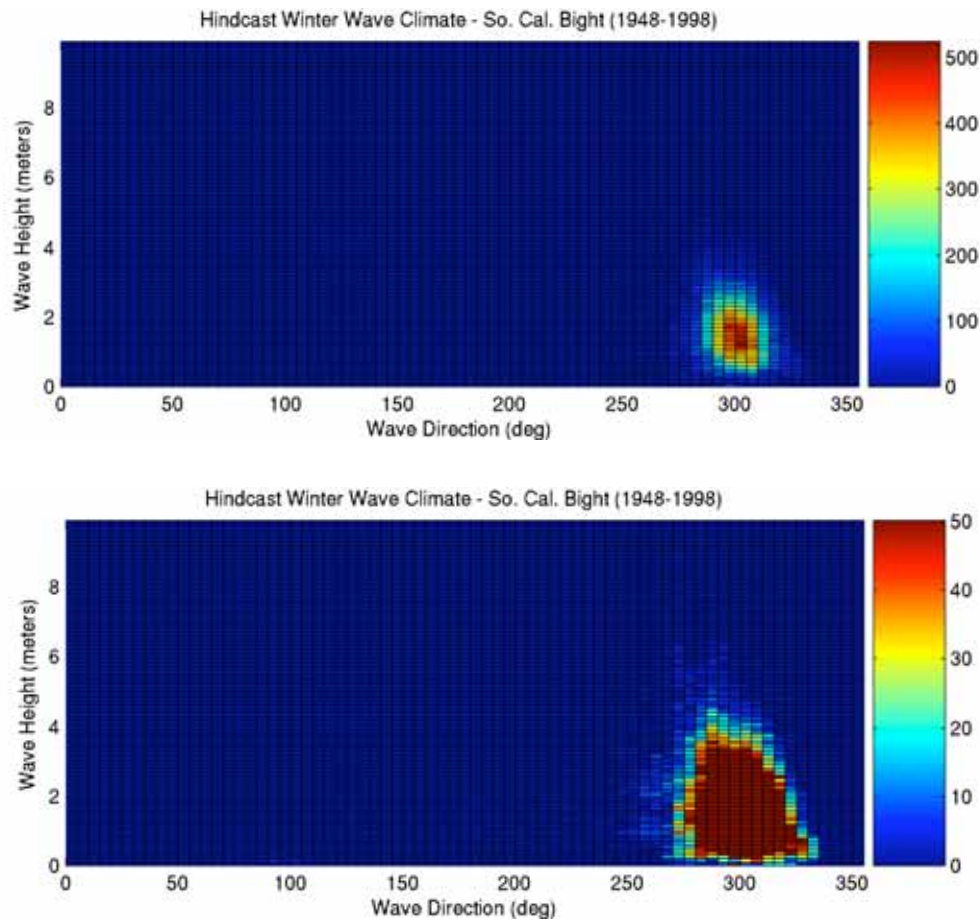
Figure 2-4. Joint distributions wave height and wave direction for the NCAR-NCEP numerical hindcast of deep-water winter wave climates (1948–1998) for location 33˚N/121.5˚W. The color map differs for each diagram to better show the spread of data distribution. Units for the color bar are counts (number of 3-hourly observations).

20
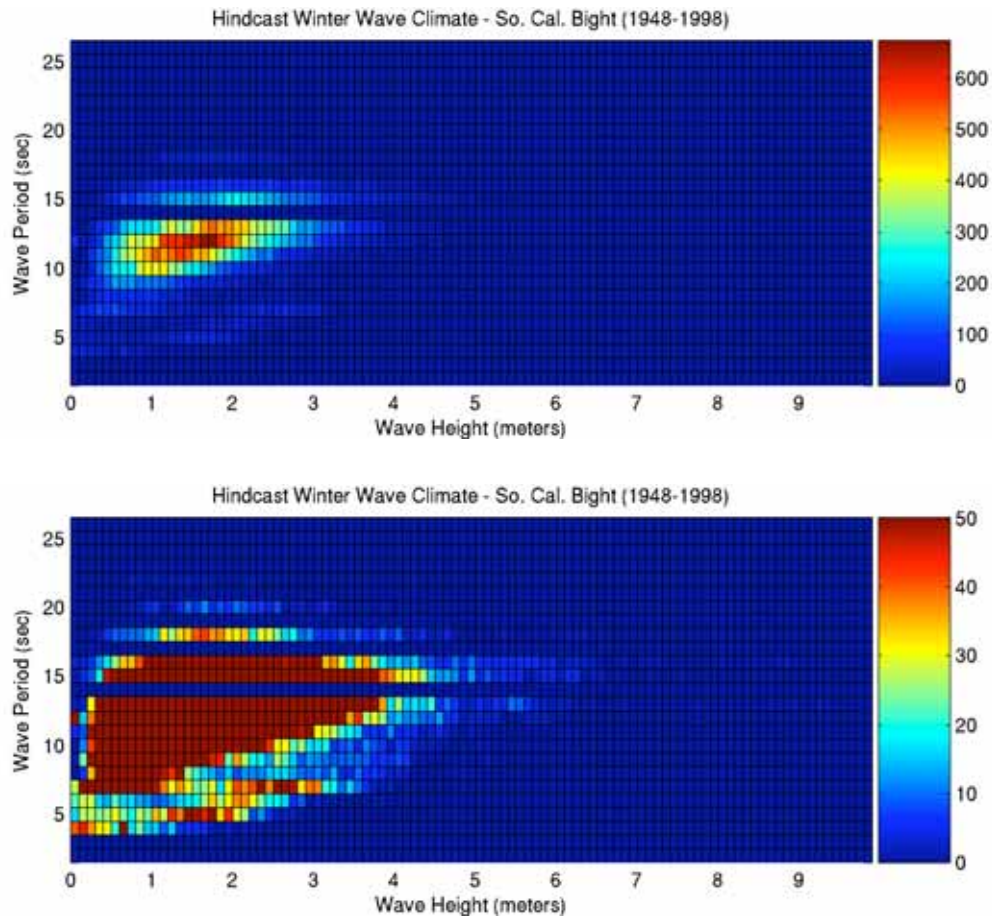
Figure 2-5. Joint distributions wave period and wave height for the NCAR-NCEP numerical hindcast of deep-water winter wave climates (1948–1998) for location 33˚N/121.5˚W. The color map differs for each diagram to better show the spread of data distribution. Units for the color bar are counts (number of 3-hourly observations).

The product of each variables' number of conditions (11*12*28) is the total number of permutations of wave triplets. The total number of SWAN main grid runs executed for the current sea level state was 3,696. For each main grid wave triplet condition, five nested grids were executed, resulting in 18,480 nested grid runs. Then all of the described offshore wave triplet inputs were re-run at a +1 meter sea level condition, resulting in a grand total of 44,352 SWAN model runs of wave transformation.

2.3.2. Wave Input Snapping

Utilizing a proxy wave climate and evenly spaced conditions of wave height, period, and direction in the aforementioned lookup tables requires that slight approximations will be made when attempting to simulate historical wave conditions. However, these approximation errors are most egregious, by percent of actual value, for low values of wave height and period. Fortunately, at these low values, longshore sediment transport is minimal. We expect few, if any, computation errors to arise from the "approximated" wave input time series, when compared to the "actual" time series. Figure 2-8 shows an example of the hindcast wave time series and its synthesized approximation through use of the SWAN lookup table.
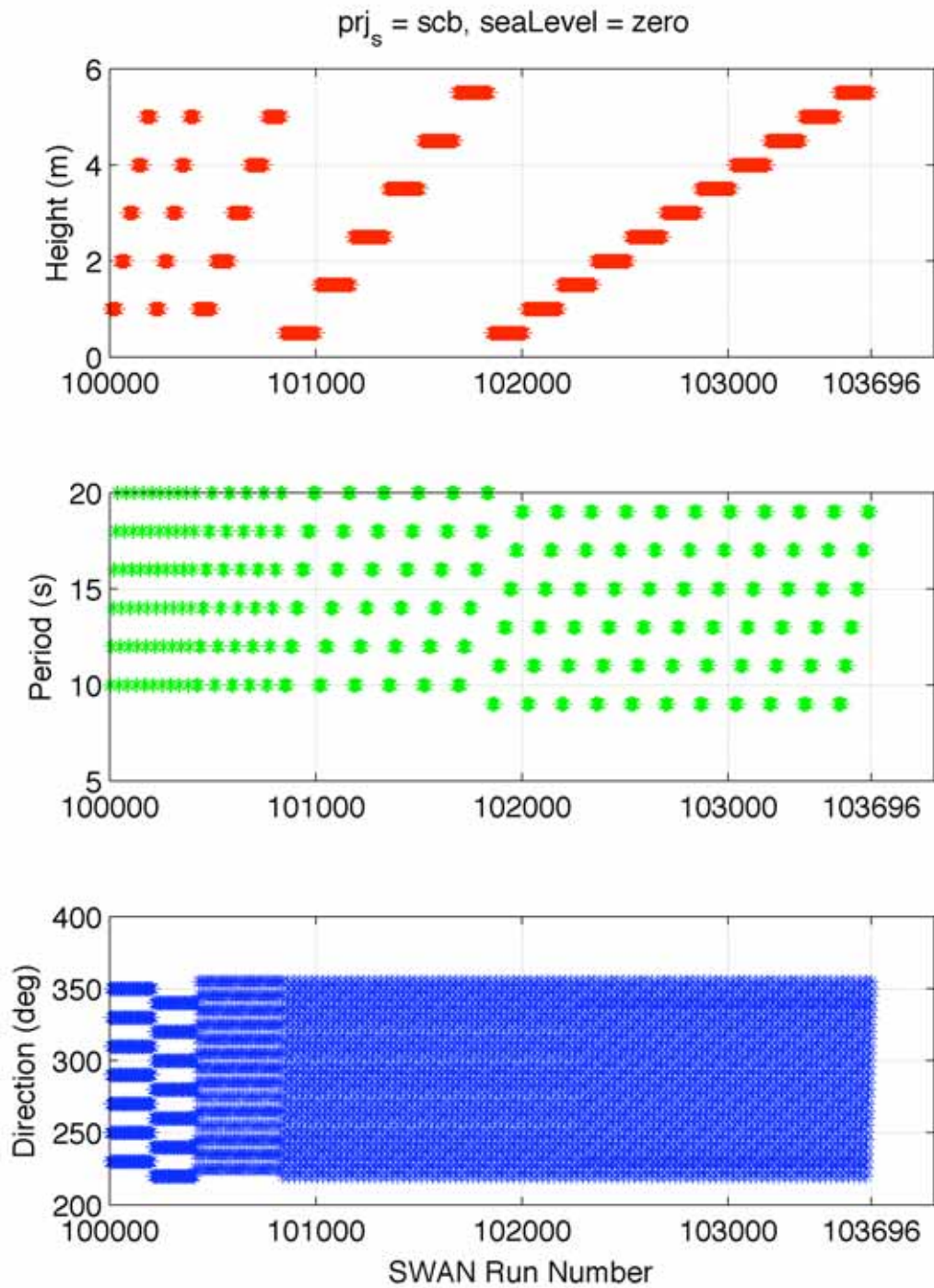
Figure 2-6. Proxy wave input conditions and corresponding SWAN run numbers for the SWAN lookup table at modern sea level
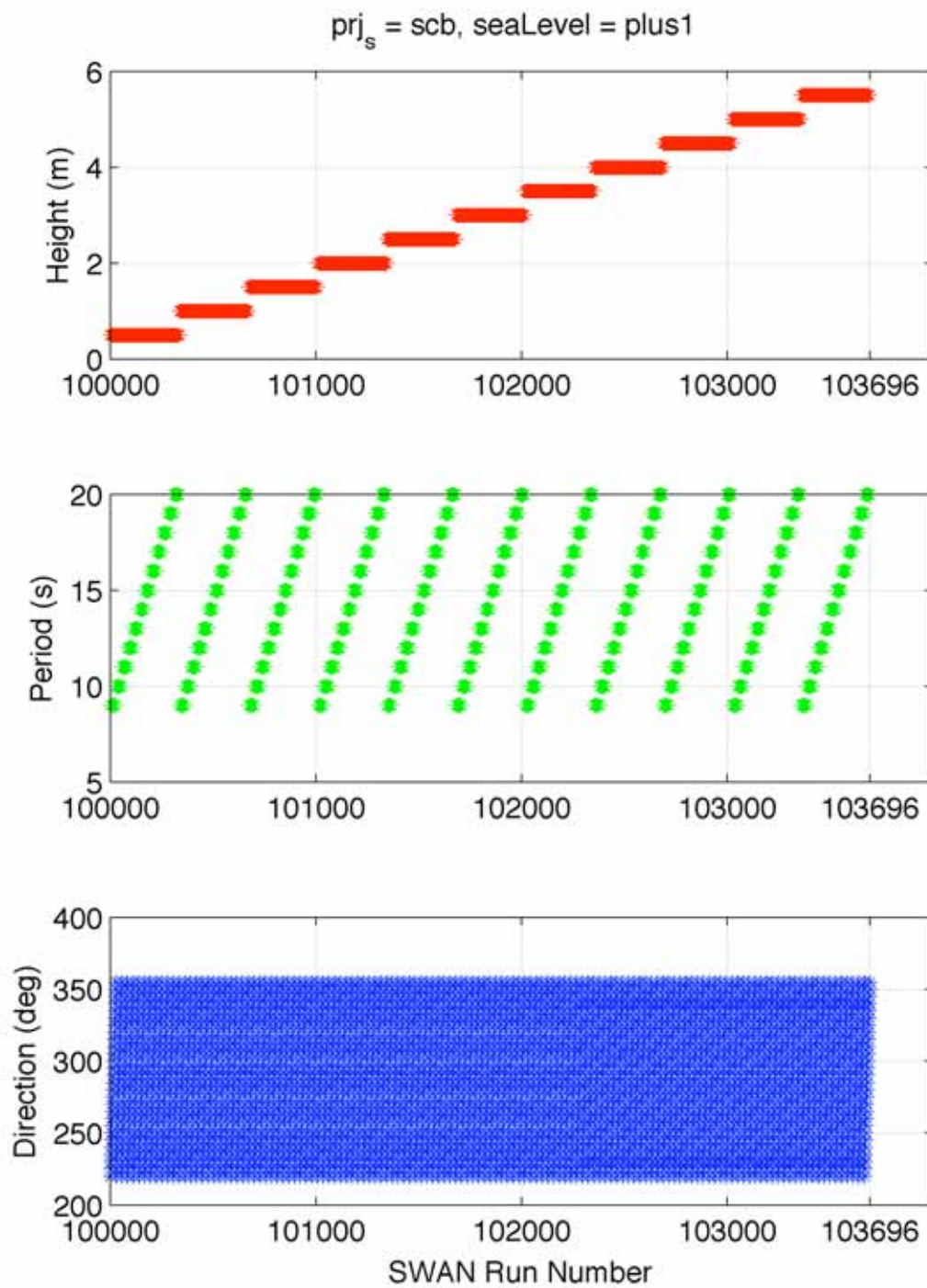
Figure 2-7. Proxy wave input conditions and corresponding SWAN run numbers for the SWAN lookup table at +1 meter sea level

23
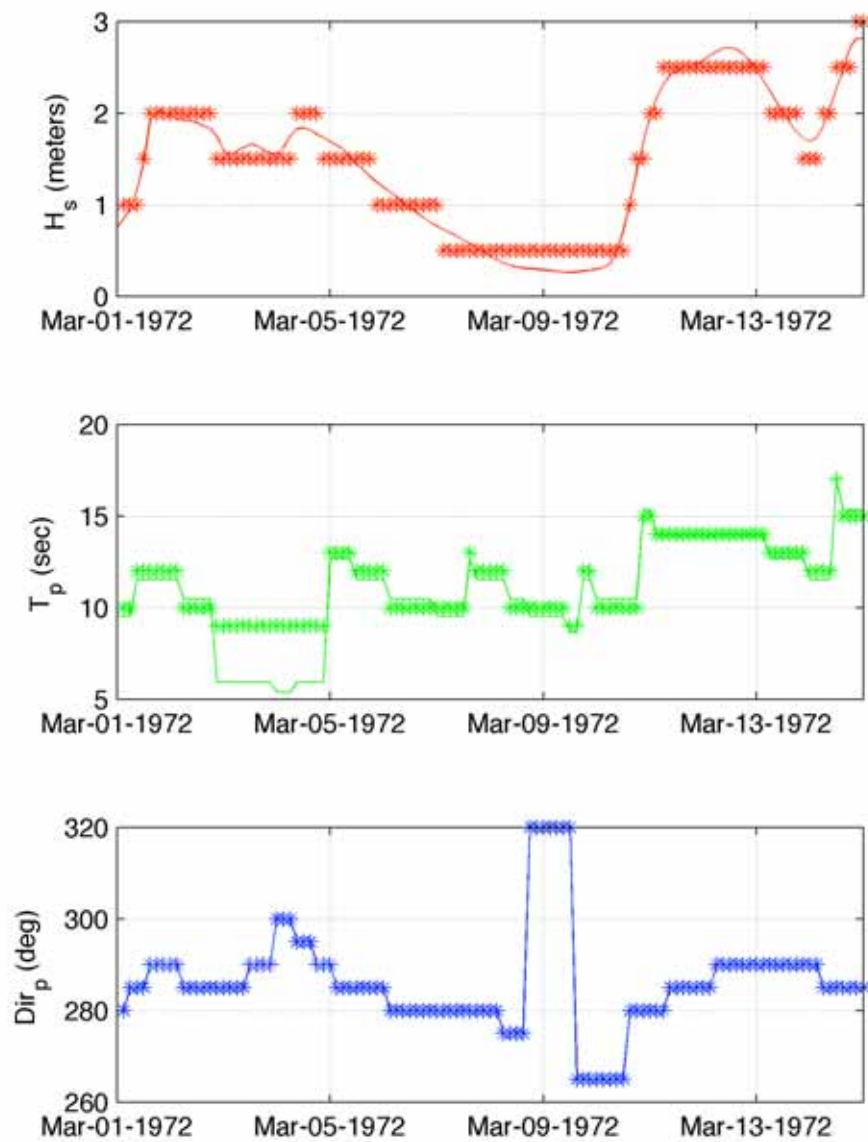
Figure 2-8. Comparison of hindcast input wave time series (shown as solid lines), with "snapped" time series (colored asterisks) using proxy wave climate generated for the SWAN lookup table

2.3.3. Far Field Grid Wave Field Computation (Coarse Resolution)

Figure 2-9 provides examples of the SWAN computation for the entire Southern California Bight wave field, under various wave height and period conditions for a northwesterly wave direction. These simulations are run at the coarse resolution of 30 arc-seconds, or approximately 1 km grid spacing. Notice the prominent sheltering effects of the Channel Islands. Also apparent in these simulations is the profound effect of wave period on refraction (wave steering in shallow water); a point that will be revisited during analysis of the numerical experiment results later in this paper.
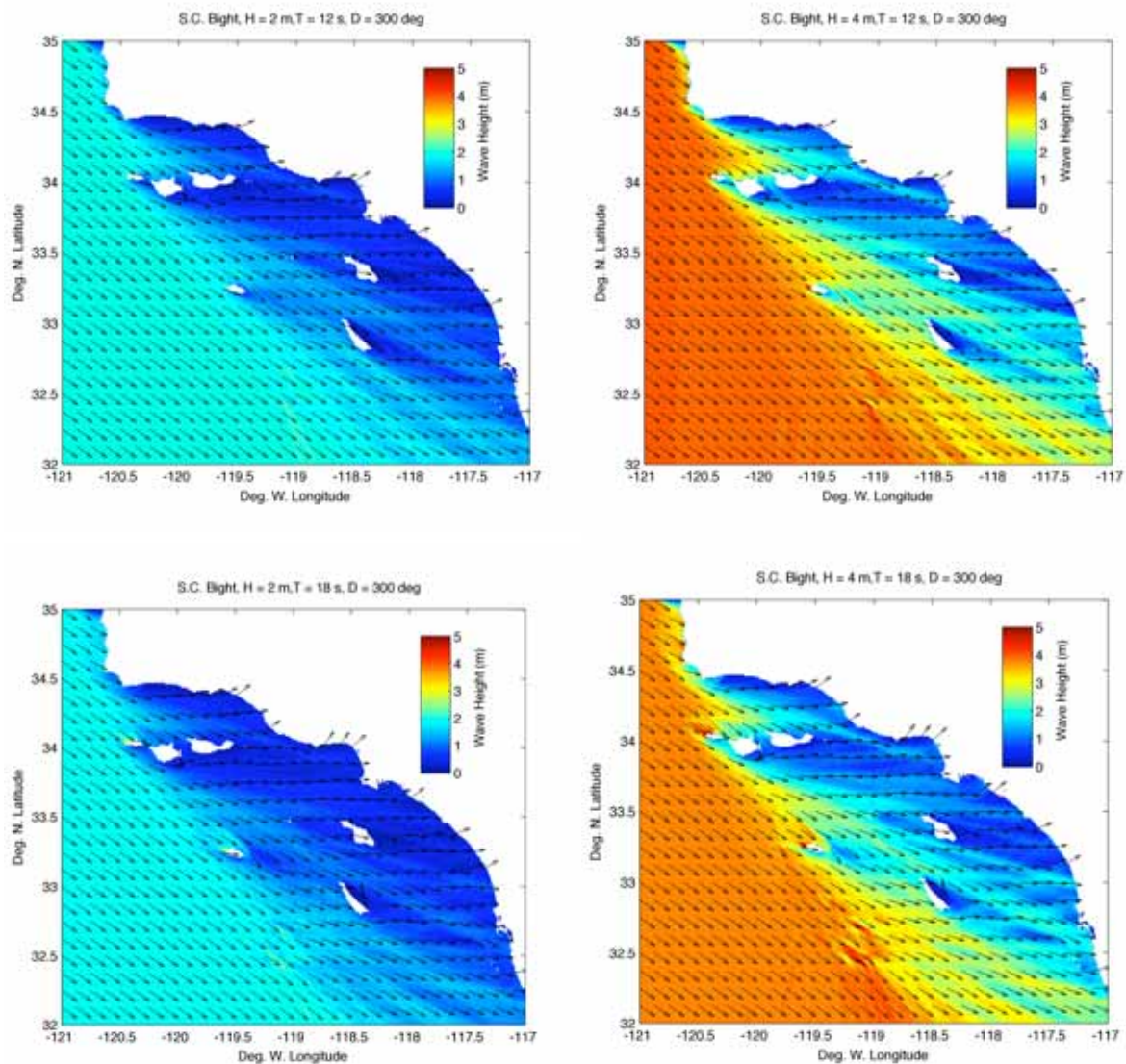
Figure 2-9. Example SWAN runs showing wave height distribution over the entire Southern California Bight, for four separate sets of offshore wave conditions. Notice the sheltering effect of the Channel Islands.

2.3.4. Near-field Grid Wave Field Computation (Fine Resolution)

Figure 2-10 provides examples of the SWAN computation for the Santa Barbara nested grid within the northern portion of the Southern California Bight wave field. These simulations are run at a fine resolution of 3 arc-seconds, or approximately 90-meter grid spacing. As in the case of the main grid above, arrows on the diagram illustrate wave ray direction, which further underscores the effect of wave period on the steering of wave rays due to refraction in shallow water.
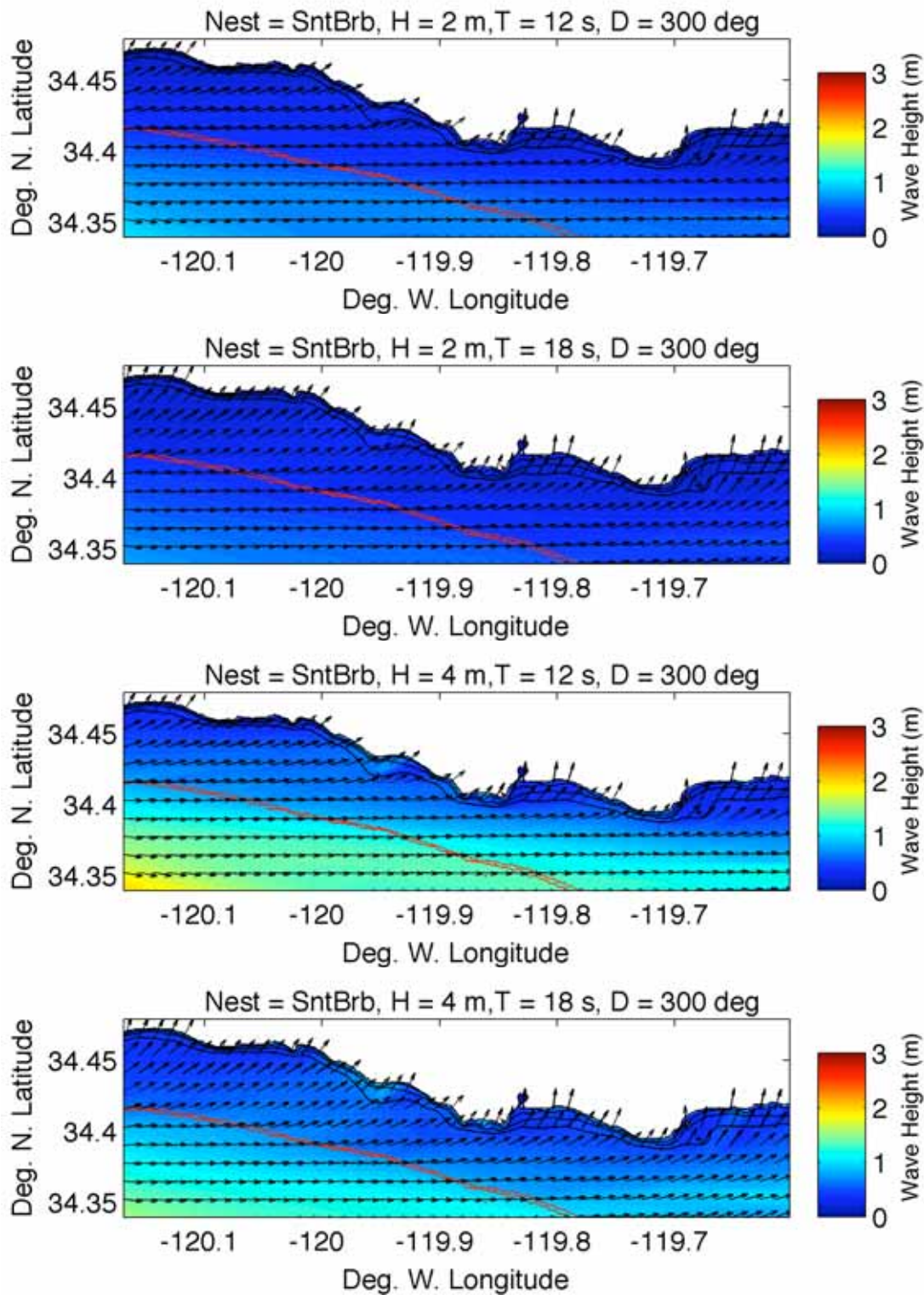
Figure 2-10. Example SWAN runs showing wave height distribution over Santa Barbara nest within the northern portion of the Southern California Bight, for four separate sets of offshore wave conditions

27

2.4.   Longshore Sediment Transport Modeling

The final output from the SWAN component of the coastal evolution model is a complete oceanic grid of significant wave heights and directions (Hs and D, respectively) at each "wet node" within the model domain. In accordance with the physics of wave transformation, wave period does not change throughout the computational grid. The task of the CGEM component of the coastal evolution model is to convert the modeled wave field into the alongshore distribution of regions of sedimentary erosion and accretion, i.e., the locations and magnitudes of erosional "hotspots." In subsections 2.4.1–2.4.8 below, we provide the details of these calculations and illustrate the numerical steps necessary to go from a nearshore wave field to a calculation of coastal erosion potential. For the sake of continuity, we will develop an example case calculation of coastal erosion potential for an instantaneous set of wave conditions.

We note that the specific form of the equation for longshore sediment transport used herein is just one of several possible options that have been developed by researchers in recent years. Various other formulations of longshore sediment transport are available and can easily be substituted into our CGEM modular-based model. Examples of the range of longshore sediment transport formulations include Inman and Bagnold (1963), Komar and Inman (1970), the CERC (Coastal Engineering Research Center) equation (Rosati et al. 2002), Kamphuis et al. (1986), Kamphuis (1991), and Bayram et al. (2007). We chose the Komar and Inman (1970) sediment transport formulation, later updated by White and Inman (1989), as it was developed from direct measurements along the California coast, thereby appropriately accounting for the regional wave climate and sedimentary character of the region considered in this study.

2.4.1.   Choosing the 5-meter Isobath

The first step is to select a consistent location at which to query the SWAN modeled wave field. Ideally, this selection should be based on the point of wave breaking, when the shoaling wave releases its energy by breaking and converts the broken wave energy to nearshore currents. However, the depth at which wave breaking occurs is dynamic, being highly dependent on the wave steepness, which has both wave height and period dependence (Kaminsky and Kraus 1993). Typical ranges for breaking depths are 8 to 2 meter water depth, as calculated by the relationship provided in Komar and Gaughan (1972). To avoid this complication, we select the 5-meter isobath as the location at which we query the SWAN results and discuss this model limitation in Section 2.5 below.

In the CGEM model, this is done by numerical routines, which apply MATLAB's contouring algorithm to each of the bathymetric nests (SntBrb, SntMnc, SnPdro, DanaPt, and TorPns) to locate the map view coordinates of the 5-meter isobath. The uncorrected 5-meter isobath locations must then be quality-checked by the user, to remove closed contours in the nearshore, and distant "anchor points" that MATLAB establishes to reference the reported contour position locations. Some degree of correction must be conducted for each specific nest, as shown in the examples provided in Figures 2-11 and 2-12.
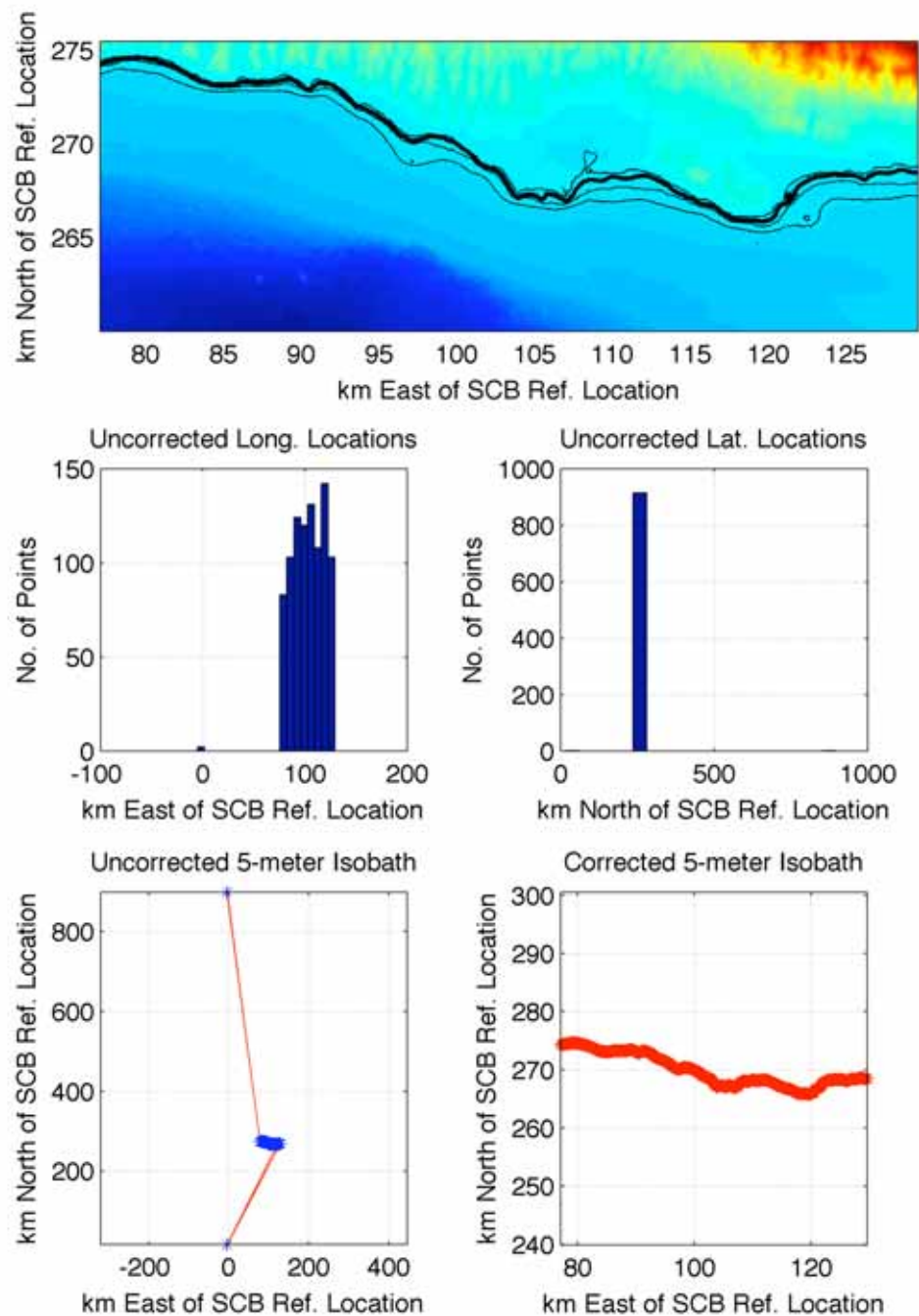
Figure 2-11. Example of selection and corrections of 5-meter isobath locations within the Santa Barbara nest. "Uncorrected" panels (histograms and map view) show outlier points generated by MATLAB's contouring algorithm. Outlier points are removed to construct "Corrected" 5-meter isobath locations.

29
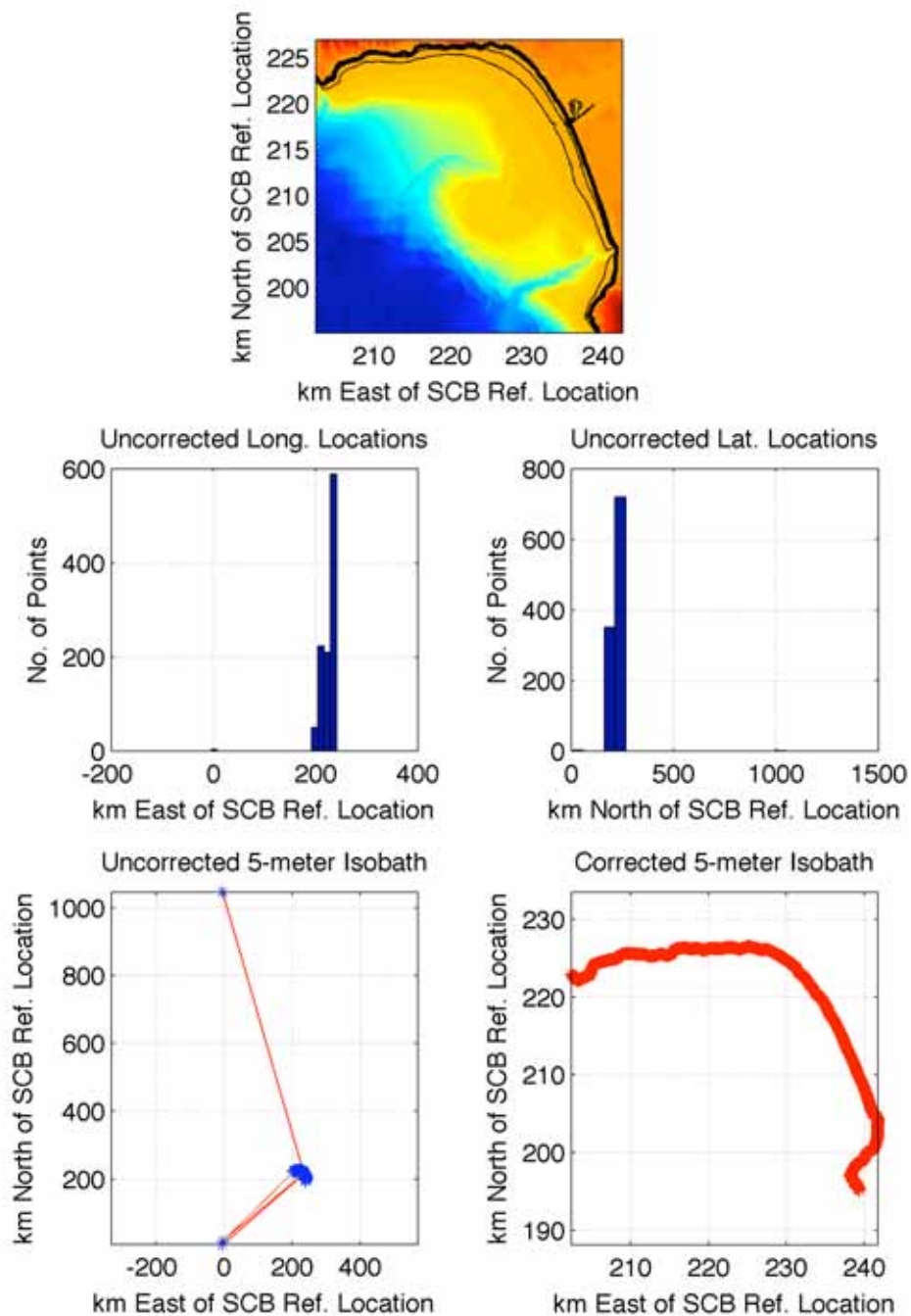
Figure 2-12. Example of selection and corrections of 5-meter isobath locations within the Santa Monica Bay nest. Details explained in caption of previous figure.

2.4.2. Decimating Along the 5-meter Isobath

After the corrected, 5-meter isobath is chosen for each nest, a consistent spacing along the isobath must be calculated, so as to have an even alongshore distribution of modeled nearshore wave conditions. For the numerical experiments presented herein, we selected a decimation spacing of 100 meters, yielding 586, 695, 357, 574, and 406 along-isobath model output positions for nests SntBrb, SntMnc, SnPdro, DanaPt, and TorPns, respectively. An example of the isobath decimation is provided for nest TorPns in Figure 2-13.
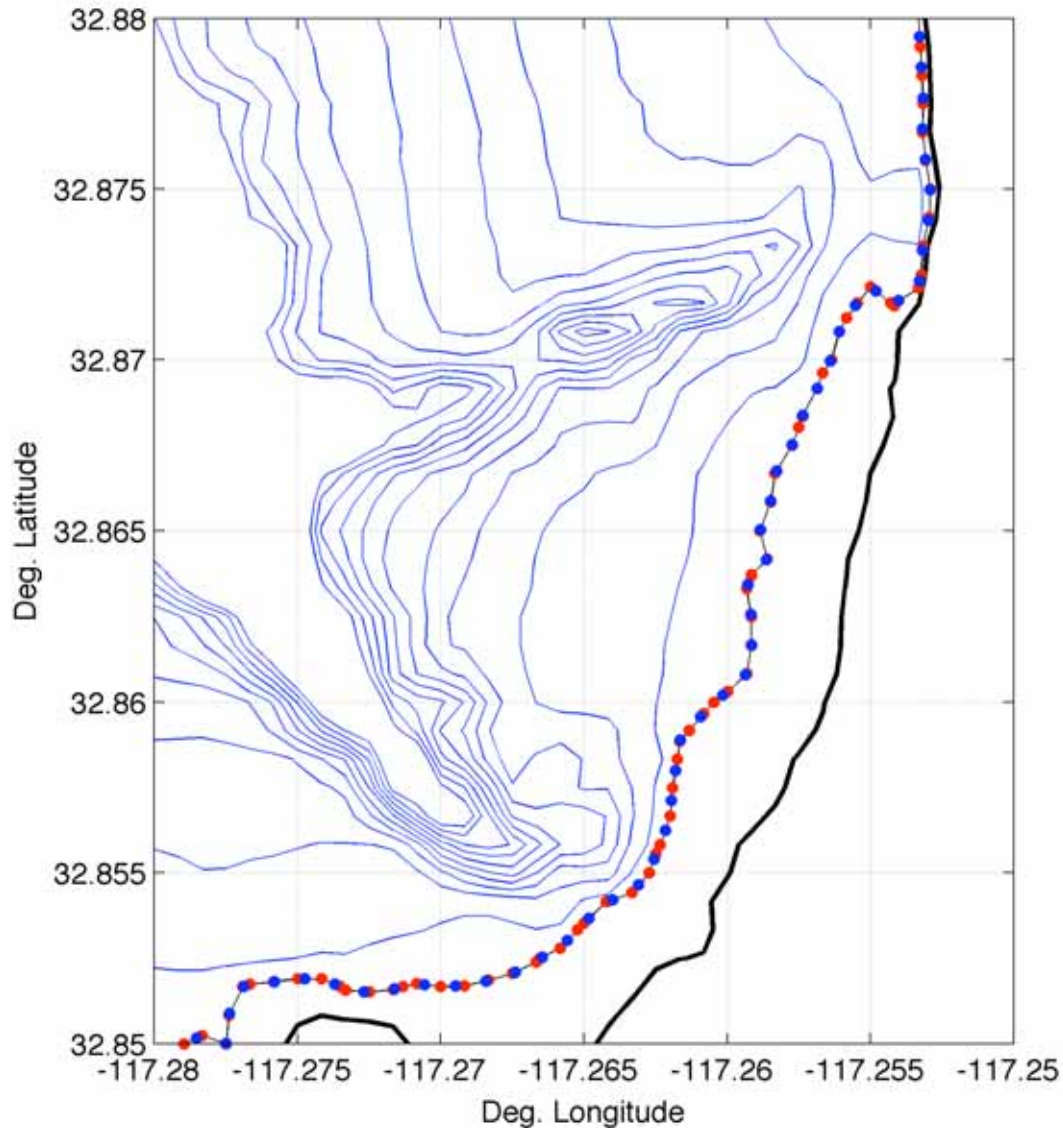
Figure 2-13. Example of 100-meter decimation of model output positions along the 5-meter isobath within the southern portion of the TorPns nest. Blue contour lines represent bathymetry at depths 10 m to 100 m, with a 10 m contour interval. Red dots show locations of original non-uniformly spaced 5-meter isobath contour

31

positions. Blue dots show locations of decimated model output positions. The thick black line shows the modern shoreline position.

2.4.3. *Computing Coastal Trends*

An accurate measurement of the orientation of the coastline is necessary for the computation of angle of incidence (α)—the difference between nearshore wave direction and coast normal direction, which is a fundamental variable in the calculation of both the radiation stress (Sxy) and the longshore component of wave energy flux (Pl), also known as the stress-flux factor. Detailed computation of coastal trends for the decimated 5-meter isobaths in each of the nested grids was performed by the following procedure:

- Starting at the northwest-most portion of the isobath, window 10 adjacent, decimated model output positions as a subset (~1 km).

- Fit a linear regression orientation line to the subset, using the widest range spatial orientation (latitude or longitude) as the independent variable. This ensures that shorelines with a more north-south trend are fit with longitude as the independent variable and that shorelines with a more east-west trend are fit with latitudes as the independent variable.

- Record the direction of the normal to the fitted trendline (90˚ clockwise from trend) as the shore-normal value for the midpoint location of the subset.

- Slide the window downcoast (toward the southeast) by one model output position and repeat the steps above.

Stepwise regression and correction calculations are provided in Figure 2-14. Shore normal orientations for two nested grids are plotted on maps in Figure 2-15.
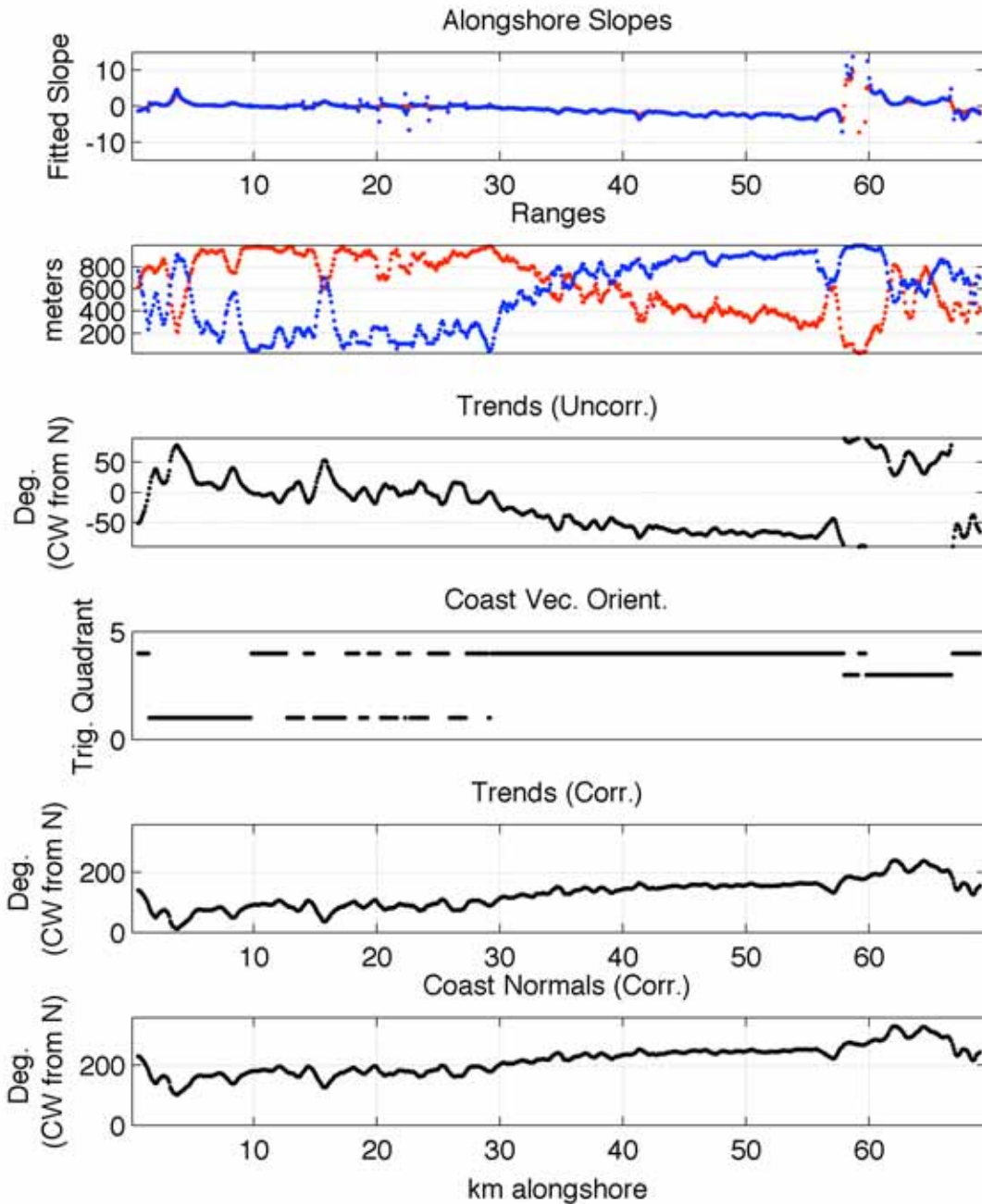
Figure 2-14. Stepwise calculation of coastal trends and coast normal orientations for Santa Monica Bay. Alongshore slopes are fitted using a least squares regression as a function of longitude (red points) and latitude (blue points). Alongshore distance range occupied by orientation-averaging window shown for longitude (red points) and latitude (blue points). Uncorrected trends are selected by selecting alongshore "slopes" associated with greater alongshore range (longitudinal vs. latitudinal). Corrected coastal trends are calculated based on

sign of trigonometric quadrant in which coastal orientation vector resides. Coast normals are orthogonal to the calculated coastal trends.
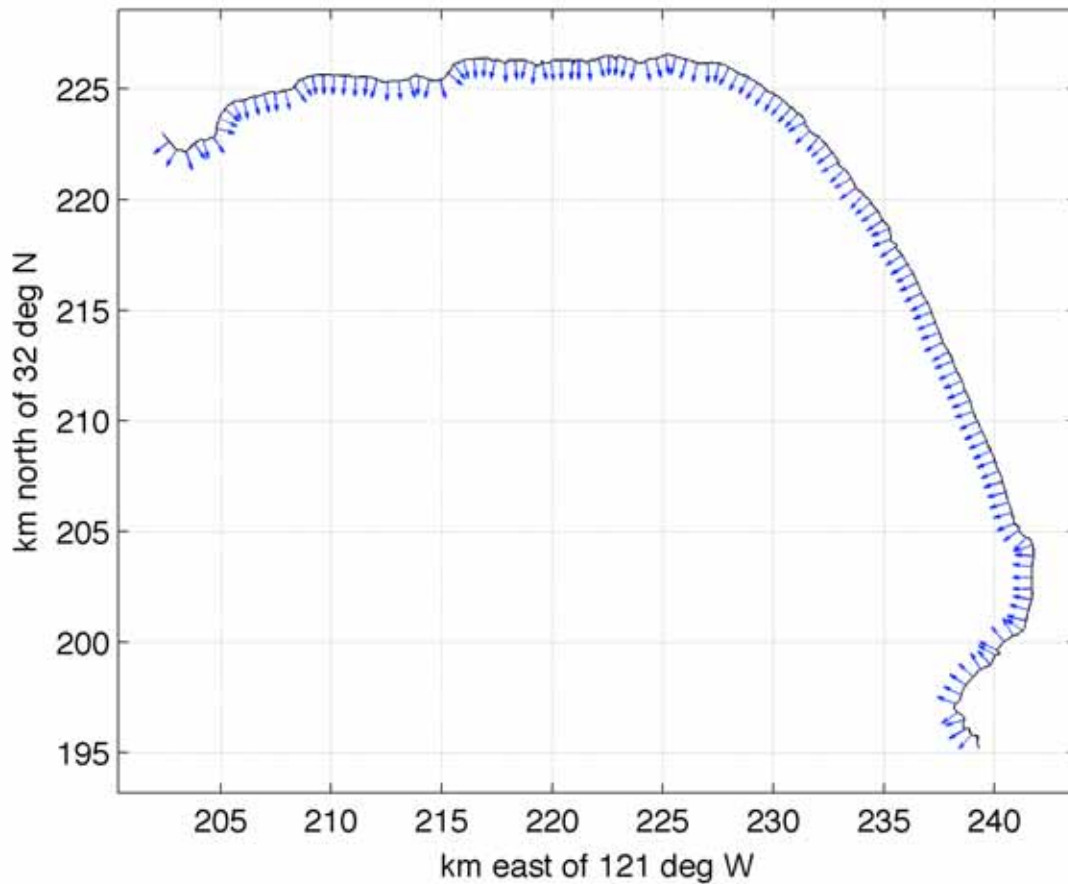
Figure 2-15. Computed coast normal orientations for the Santa Barbara region (upper panel) and Santa Monica Bay (lower panel)

2.4.4. Retrieving and Interpolating SWAN Output

The task of obtaining model output at the decimated model output positions is performed by simply conducting a two-dimensional linear interpolation of the SWAN nested grid results for wave height and direction. After retrieval, the alongshore wave heights and directions are smoothed with a 1-km moving average window.

2.4.5. Calculating Angle of Incidence

A major control on longshore sediment rate is the longshore component of wave energy flux. The angle of incidence is of primary importance in the calculation of longshore sediment transport, as will be further discussed in subsection 2.4.7. If wave rays approach the beach at an angle perfectly orthogonal to the trend of the coast, the longshore component of wave energy flux is zero, and there is no net longshore current to drive longshore sediment transport. If wave rays approach the beach at an oblique angle (somewhere between orthogonal and parallel),

there is a component of wave energy flux parallel to the shoreline, which drives longshore sediment transport.

The calculation of angle of incidence in the CGEM model is quite straightforward and proceeds as follows: Assuming a north-south trending coastline with land to the east and sea to the west, the angle of incidence is the difference between the nearshore wave direction (azimuth) and the coast normal (azimuth). Two scenarios are described below. In scenario A, nearshore waves approach from the northwest (D~300˚) and the coast normal is approximately due east, referenced by the direction from which the vector originates (N~270˚), making the angle of incidence (α) equal to approximately +30˚. Longshore currents generated for scenario A would be directed southward. In scenario B, nearshore waves approach from the slightly south of west (D~265˚) and the coast normal is approximately due east, as in scenario A (N~270˚), making the angle of incidence (α) equal to approximately -5˚. Longshore currents generated for scenario B would be directed northward, with decidedly less magnitude.

2.4.6. Calculating Wave Energy Flux

Wave energy flux P, which has dimensions of [mass•length/time^3] and units of [Watts/meter of shoreline], is calculated through the relationship

$$P = ECn = \frac{1}{8}\rho g H^2 Cn$$

where E is wave energy density, which has dimensions of [mass/time^2] and units of [joules/meter^2], C is nearshore wave celerity, which is depth controlled and has dimensions of [length/time] and units of [meters/second], n is ratio of group to individual wave speed (~1 in shallow water) and is dimensionless, ρ is the density of seawater [1024 kg/m^3], g is gravitational acceleration [9.81 m/s^2], and H is nearshore wave height, which has dimensions of [length] and units of [meters], as computed by the SWAN portion of the model and interpolated along the decimated 5-meter isobath.

The longshore component of wave energy flux, P_l, is calculated by simply multiplying the wave energy flux, P, by the trigonometric functions that provide the component parallel to shore

$$P_l = P \sin\alpha \cos\alpha$$

where the sine and cosine terms result from the tensor transformation of the onshore flux of longshore directed momentum that is embedded in P_l (Longuet-Higgins and Stewart 1964). Procedure for calculation of angle of incidence, α, is described in Section 2.4.5., above. Example stepwise calculations of wave energy flux for the SntMnc grid are shown in Figure 2-16.
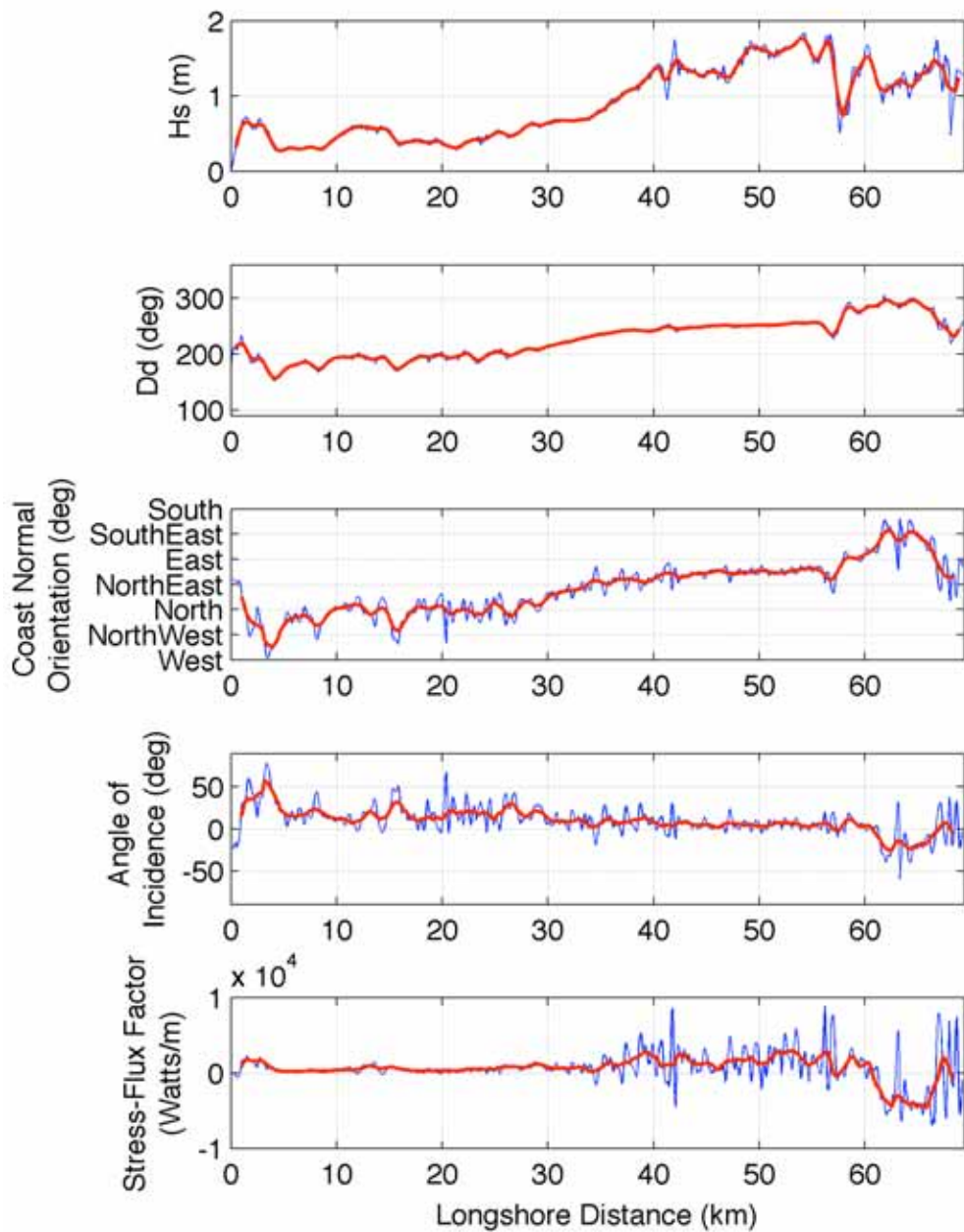
Figure 2-16. Stepwise calculations of alongshore variability of modeled wave height, modeled wave direction, coast normal orientation, angle of incidence, and stress-flux factor for an example simulation in Santa Monica Bay

2.4.7. Calculating Divergence of Drift

The formulation of longshore sediment transport calculation used in the CGEM model comes from the sediment-transport theories of Bagnold (1963), Inman and Bagnold (1963), and Komar

36

and Inman (1970). These theories utilize the concept of immersed-weight sediment transport rate (I_l) to account for density of sediment grains,

$$I_l = K_l P_l = K_l [P \sin\alpha\cos\alpha]$$

where K_l represents a dimensionless coefficient of proportionality, as defined by Komar and Inman (1970), and is set to a value of 0.8 for all of the numerical experiments described below. Immersed-weight transport rate is converted to volumetric transport rate through the relationship

$$Q_l = \frac{I_l}{(\rho_s - \rho_w)gN_o}$$

where ρ_s and ρ_w are densities of quartz sediment (2650 kg/m^3) and seawater (1024 kg/m^3), respectively, g is the gravitational acceleration constant (9.81 m/s^2), and N_o is the volume concentration of solid grains, set to 0.6, for all numerical experiments described below.

The calculation of the volumetric rate of longshore sediment transport yields a rather noisy result. To obtain a more reasonable estimate of local trends in longshore sediment transport, we smooth the calculations of longshore transport with a 1-km moving average window (Figure 2-17).
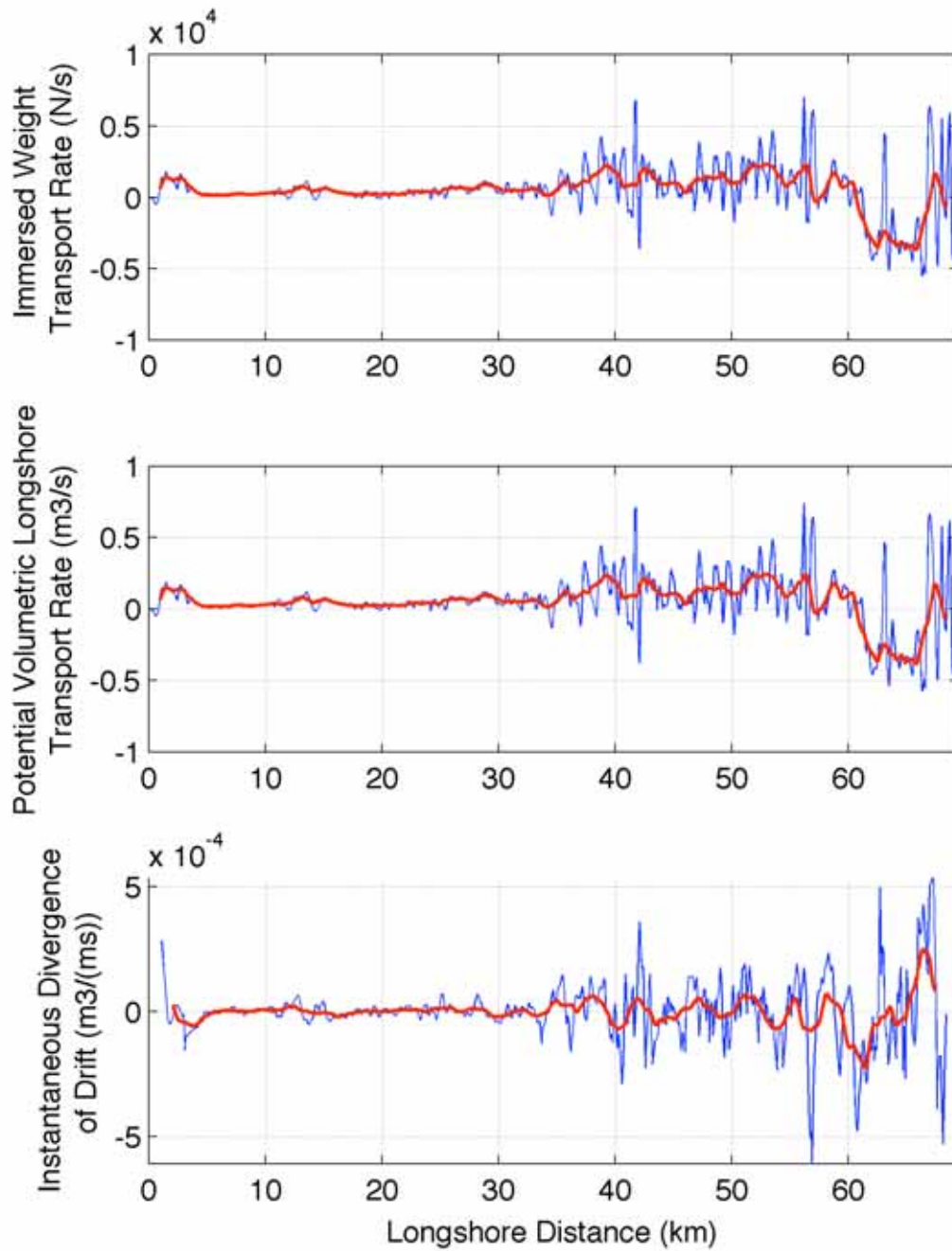
Figure 2-17. Example calculation of longshore sediment transport rates and divergence of drift for Santa Monica Bay

The last remaining step to obtain volumetric estimates of gradients in longshore transport (also known as the divergence of drift) is to perform a discretized differential of volumetric rate of longshore sediment transport with respect to alongshore position.

$$\nabla \cdot Q_l = \frac{\partial Q_l}{\partial l}$$

The results of this calculation are out of phase with longshore sediment transport, as expected, illustrating regions where longshore sediment transport rate reaches a local maxima or minima correspond to regions where the divergence changing from negative to positive, or positive to negative, respectively (Figure 2-17).

2.5. Model Limitations

The use of a three-dimensional lookup table to approximate time series of wave conditions presents the drawback that precise conditions are not used as inputs for deep-water wave conditions in the SWAN wave transformation calculations. Although this is an approximation, we have set the interval spacing for wave heights, periods, and directions in the lookup table sufficiently small that we expect inaccuracies arising from the imprecision of inputs to be minimal.

We acknowledge the assumption that the 5-meter isobath is representative of nearshore wave conditions should be taken into account appropriately. Under conditions of milder wave fields, wave breaking will be landward of the 5-meter isobath, and for similar considerations, wave breaking under conditions of highly energetic wave fields will be seaward of the 5-meter isobath location. However, for most wave fields the break point will be landward of the 5-meter isobath, and in these cases, we can rely on the conservation of wave energy flux to protect our assumption.

It should be noted that the calculations of divergence of drift, described in Section 2.4.7, are potential divergence of drift, assuming that we have a transport-limited longshore drift scenario, meaning that we are calculating the total amount of longshore transport of sediment if an unlimited supply was available. This is not likely the case for much of the Southern California coast, as river-damming and the arid environment tends to make the littoral system supply-limited in many places. Where the wave energy demands on sediment transport exceed the supply, bedrock platforms will be exposed and erosion of sea cliffs will proceed with greater efficiency.

3.0 Numerical Experiments and Results

Given the wide range of possible numerical experiments suitable for a modeling study of the influence of climate change on coastal evolution, we designed and conducted two general experiments that employ the modeling procedure described above, for two of the chosen study sites within the Southern California Bight (Sections 3.1 and 3.2). In addition, we have assembled a section that demonstrates a procedure to calculate sea cliff retreat in response to sea level rise (Section 3.3). The first experiment examined the effect of wave direction on magnitude and location of longshore drift divergence along the eastern portion of the Santa Barbara County coast. The second experiment conducted is a probabilistic evaluation of likelihood for erosional hotspot development along the coast of Los Angeles and Orange Counties given the known

frequency of El Niño winters and Pacific Decadal Oscillation over the past half-century. Lastly, the procedural demonstration shows how sea cliff retreat can be expected to occur as a result of an elevated eustatic sea level, driven by global climate change, for the central coast of San Diego County.

The three specific study sites, selected for the three sets of numerical experiments ⁄ demonstrations, represent three distinct orientations with respect to the Pacific Ocean: (1) east-west trending, south-facing coast (the eastern reach of Santa Barbara County coast – "SntBrb"), (2) cuspate shaped with smoothly varying orientation from south-to-west facing coast (the Santa Monica Bay and Orange County coasts – "SntMnc," "SnPdro," and "DanaPt"), and (3) north-south trending, west-facing coast (the central San Diego County coast – "TorPns"). Locations and close-up views of these sites are provided in Figures 1-1 and 1-2.

3.1.   Wave Direction Experiment

Before the 1980s the beaches adjacent to and east of the campus of the University of California at Santa Barbara were wide and well vegetated. A significant sedimentary barrier persisted from year to year, which protected the relatively soft sea cliffs upon which the community is built. For a well-documented photo essay of coastal change at this site, we refer the reader to the online resource maintained by Dr. Arthur Sylvester, Professor Emeritus at UC-Santa Barbara (www.geol.ucsb.edu/faculty/sylvester/UCSBbeaches.html). As the photo history illustrates, by the El Niño winter of 1982–1983, the natural protection of the beach had disappeared and storm waves had free access to inflict damage upon the base of the friable sea cliffs.

The aforementioned anecdote of severe coastal change motivated a numerical experiment to examine the effect of deep-water wave direction on the location and magnitude of coastal erosional hotspots. Our goal in this experiment was to understand how changes in deep water wave conditions drive the spatial pattern of coastal geomorphic response. Such an experiment is worthwhile because of the observations that stormier wave years, such as El Niño winters, bring more westerly wave directions than usual, in addition to the well-documented larger wave heights (see Section 2.2.2 and Adams et al., 2008). To investigate this inquiry, we selected a portion of the east-west trending, south-facing Santa Barbara coast, shown in Figure 3-1.
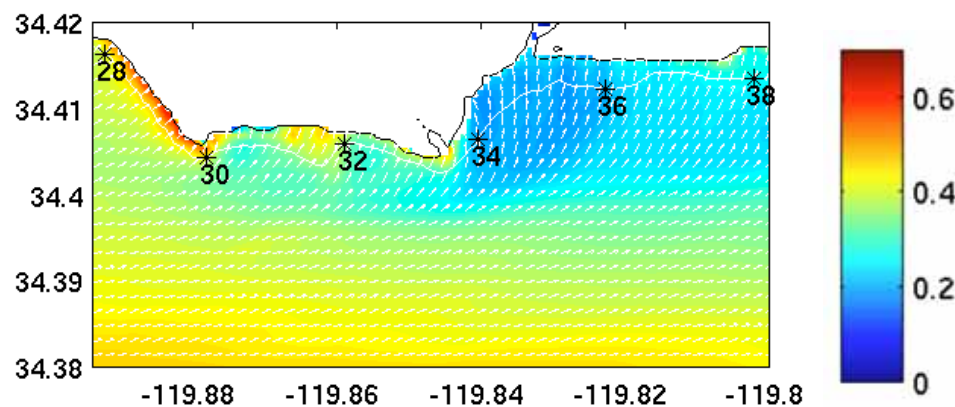
3.1.1. Experimental Design

We conducted this experiment in two parts: A and B. Part A was run as an example to compare how the spatial pattern of divergence of drift over a seven-day period can be dramatically different for two wave fields of comparable energy, but different directions. Part B was a systematic exploration of parameter space to quantify how much directionally driven change in divergence of drift is observed at two sites differing in their wave-field exposure.

We conducted part A by setting up reference SWAN-CGEM runs for two separate seven-day intervals of known deep-water wave conditions, representing a "moderate" La Niña event (December 21–28, 1988) and a "moderate" El Niño event (January 7–14, 1983), respectively. The deep-water time series of wave height, period, and direction that were used as SWAN inputs for each of these events, provided by the three-hourly numerical hindcasts of Graham and Diaz (2001), are shown in left-hand panels of Figures 3-2 and 3-3. Notably, the wave heights and periods for each of these two events are not remarkably dissimilar from one another. The wave directions, however, are quite different; the La Niña event witnesses wave directions that are more northwesterly (range: 300˚–320˚); whereas the El Niño event witnesses wave directions that are more westerly (range: 280˚–300˚).
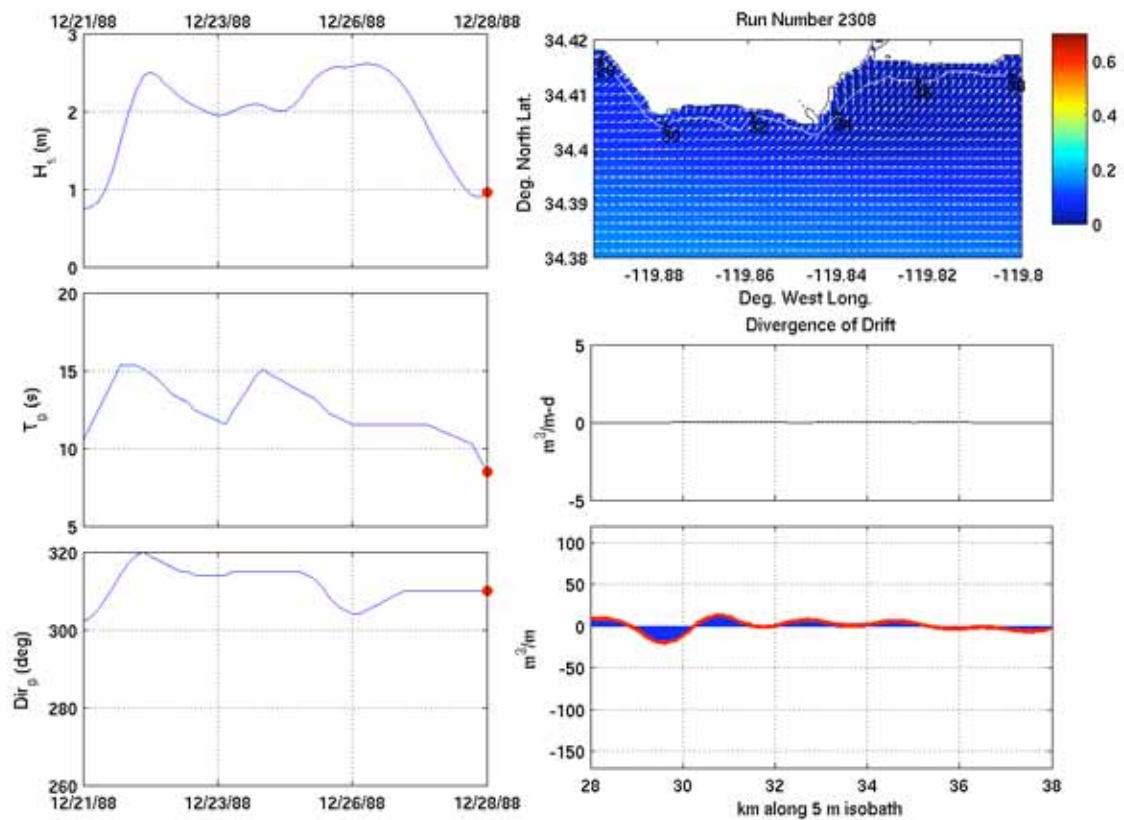
Figure 3-2. Output from a La Niña simulation, Experiment 1A, Santa Barbara coast. Upper right panel shows small nearshore waves (Hs =~0.2 m) relative to larger deep-water waves (Hs =~1.0 m); an effect of >90 degrees of refraction around the sheltering peninsula for northwesterly waves.
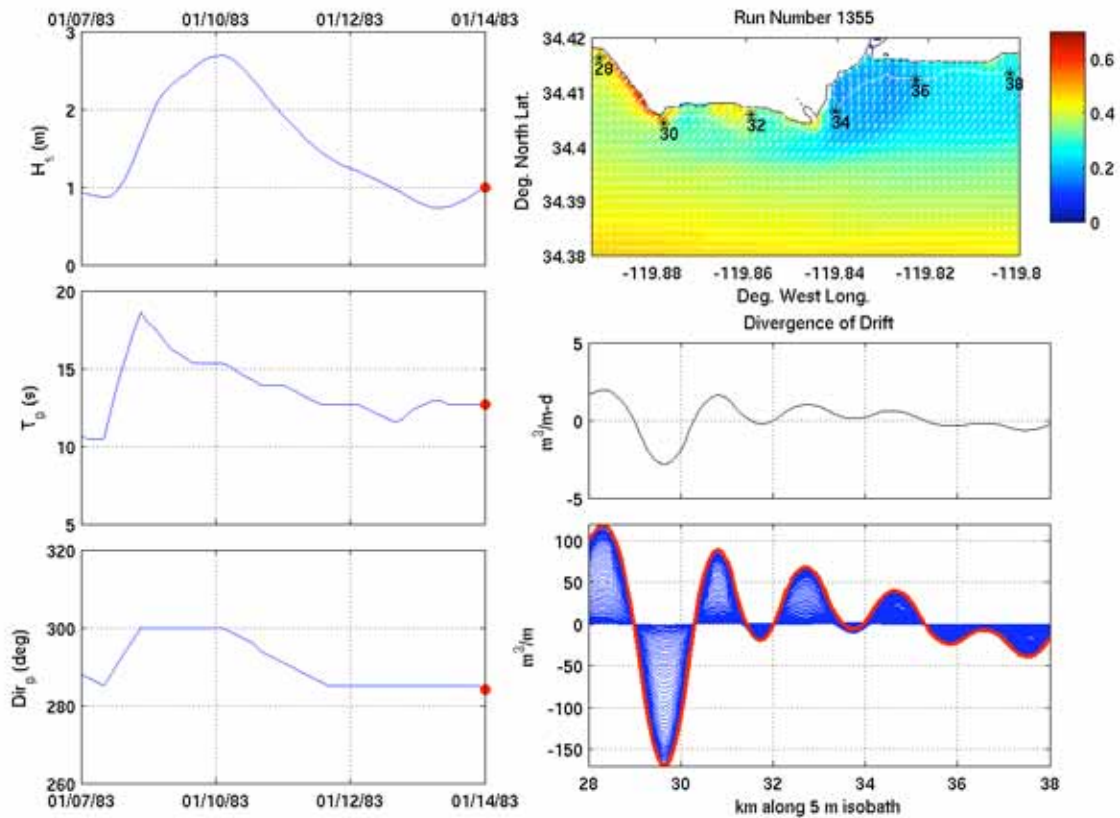
Figure 3-3. Output from an El Niño simulation, Experiment 1B, Santa Barbara coast

We conducted part B by setting up SWAN-CGEM runs for three deep-water wave height/period pairs, systematically varying deep-water wave direction from northwest (320˚) to slightly south of due west (260˚) with an interval spacing of 2˚. This resulted in 90 total SWAN runs for the nested Santa Barbara coastline. Table 3-1 shows the three wave height-period pairs selected for part B of the wave direction experiment.

Table 3-1. Input values for 90 SWAN runs performed in the Santa Barbara wave direction experiment

Name of Height/ Period Pair	Deep-water significant wave height, $H\infty$ (m)	Deep-water peak wave period, Tp (s)	Range of deep-water dominant wave direction, α (˚)
Moderate Heights/ Moderate Periods	2	12	260 : 2 : 320
Extreme Heights/ Moderate Periods	4	12	260 : 2 : 320
Extreme Heights/ Long Periods	4	16	260 : 2 : 320

The two locations examined in detail were (1) an exposed, southwestward-facing, rocky point, known as Coal Oil Point, shown at kilometer marker 30 in Figure 3-1, and (2) the sheltered, eastward-facing, University of California, Santa Barbara (UCSB)-Goleta beach location (referenced in the photo history by Sylvester mentioned above), shown at kilometer marker 34 in Figure 3-1. For each of the two locations, we modeled the divergence of drift (i.e., erosional/accretional hotspot potential) for the deep-water wave height/period pairs and range of wave directions listed in Table 3-1.

3.1.2. Results

The results of part A of the Santa Barbara wave direction experiment are shown in right-hand panels of Figures 3-2 (La Niña event) and 3-3 (El Niño event). The reference maps (upper right panels of Figures 3-2 and 3-3), show the location of the 5-m isobath, kilometer markers along the isobath (28–38), and the wave height field for the final SWAN simulation, whose input conditions are specified by red dots on adjacent time series of inputs. The alongshore distribution of longshore divergence of drift for the final SWAN simulation is presented in the middle right-hand panels of Figures 3-2 and 3-3. In the lower right-hand panels of Figures 3-2 and 3-3, the cumulative divergence of drift for each of the seven-day events is shown as a bold red line enveloping the modeled accretion/erosion history for the coastal reach.

The results of part B of the Santa Barbara wave direction experiment are compiled in Figure 3-4. Each asterisk (*) or circle (o) on Figure 3-4 represents a unique SWAN-CGEM model run for a proscribed triplet of SWAN inputs for deep-water wave height (H), peak period (T), and dominant direction (D).
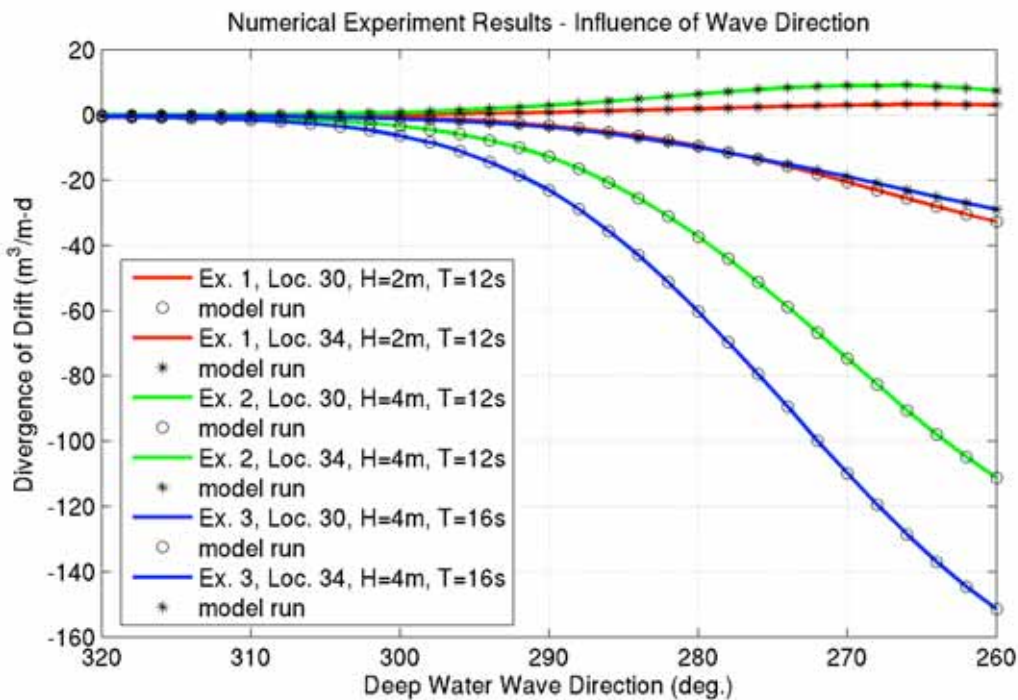
Figure 3-4. Results of 90 SWAN-CGEM runs exploring effect of wave direction on divergence of drift at sheltered and exposed locations within the Santa Barbara nest

3.1.3. Experimental Conclusions and Implications

From the wave direction experiments, the following conclusions can be drawn:

1. Variation of Erosional/Accretional Response for Exposed vs. Sheltered Coast Locations: A 30˚ difference in deep-water wave direction (300˚ vs. 270˚) can result in an order of magnitude difference in divergence of drift for exposed locations (Site 30). Wave period can alter the effect of wave direction on divergence of drift at a sheltered site, wherein nearshore sedimentary behavior can change from dominantly accretional to dominantly erosional (Site 34).

2. Influence of Wave Height on Directionally Affected Divergence of Drift: At moderate wave periods, doubling of the wave height changes the directional effect on divergence of drift by 300%, for an exposed coastal location (Site 30).

3. Influence of Wave Period on Directionally Affected Divergence of Drift: At extreme wave heights, a 33% increase in wave period changes the directional effect on divergence of drift by 35%–40%, for an exposed coastal location (Site 30).

4. Aside from the change from accretional to erosional nearshore sedimentary behavior for an increased wave period, it appears that divergence of drift at the sheltered site is less sensitive in magnitude to variation in deep water wave direction than at the exposed site. This conclusion is drawn by comparing differences between red and green asterisk model runs with differences between red and green circle model runs.

5. A key implication from this experiment concerns patterns of storminess and climate change. Recent evidence suggests that El Niño frequency has increased commensurate with warmer global climates. During El Niño wave events, wave direction is more westerly and of longer period than during non-El Niño conditions. This increased frequency of "Pineapple Express" events will increase potential divergence of longshore drift at exposed sites by as much as 300%, as shown in this experiment.

3.2. Erosional Hotspot Likelihood Experiment

The second set of experiments targets a probabilistic evaluation of likelihood for erosional hotspot development along the coast of Santa Monica Bay, given the known frequency of El Niño winters and Pacific Decadal Oscillation over the past half-century. Using the aforementioned numerical hindcast of Graham and Diaz (2001) for deep-water winter wave heights, periods, and directions for the period 1948–1998, we use the SWAN-CGEM model to calculate estimates of annual potential beach volume change for 14 specific beaches within the Santa Monica Bay region. Results from this experiment will give a modeled history of locations of erosional hotspots for the years 1948–1997. We selected these beaches on the basis of their utility for the coastal economics study by Pendleton et al. (2008), sponsored by the California Energy Commission's Public Interest Energy Research (PIER) Program. The names and locations of the beaches are provided on the maps in Figure 3-5 and in Table 3-2.
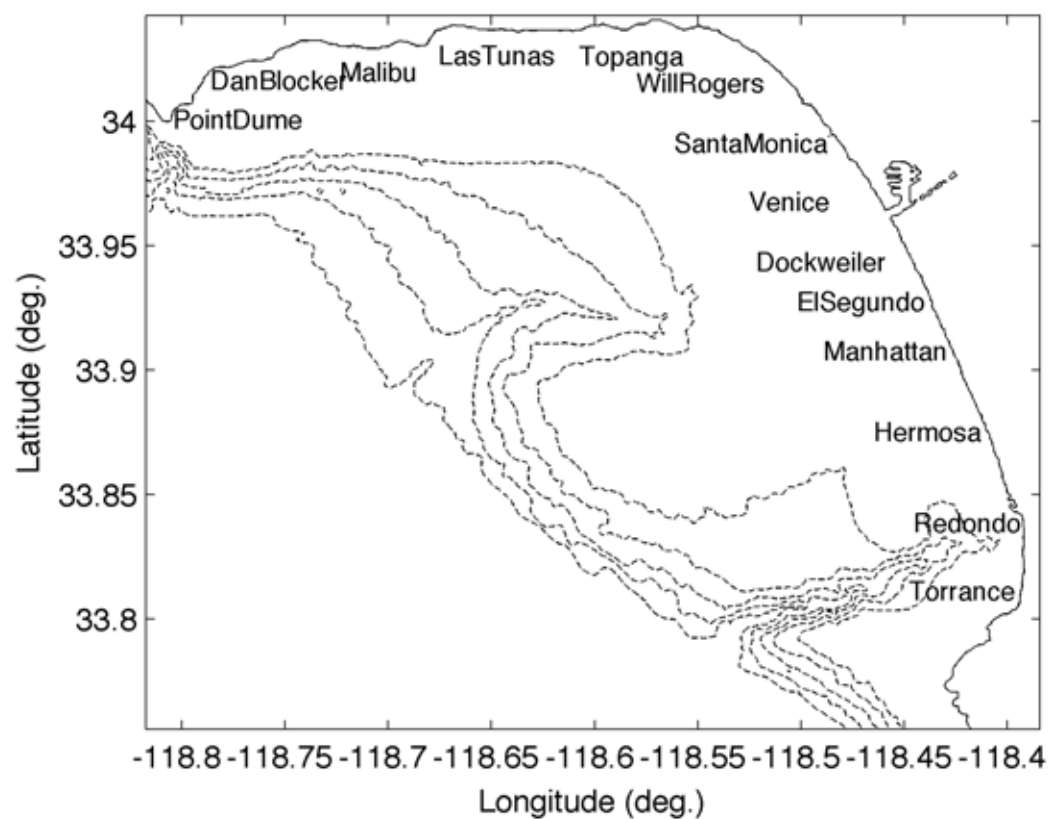
**Figure 3-5. Location maps for Experiment 2 beaches within the nest "SntMnc."
The bathymetric contour interval is 100 m to a depth of 500 m.**

Table 3-2. Names, lengths, and locations of beaches examined in the Santa Monica Bay beaches erosion/accretion likelihood analysis

Beach Name	Beach Length (km)	Longitude NW end	Latitude NW end	Longitude SE end	Latitude SE end
PointDume	6.3	-118.8042	34.0007	-118.7531	34.0260
DanBlocker	2.8	-118.7524	34.0267	-118.7244	34.0299
Malibu	5.4	-118.7233	34.0298	-118.6718	34.0363
LasTunas	4.0	-118.6188	34.0367	-118.5828	34.0358
Topanga	2.6	-118.5819	34.0362	-118.5559	34.0354
WillRogers	1.7	-118.5484	34.0355	-118.5319	34.03
SantaMonica	6.2	-118.5312	34.0294	-118.4866	33.9933
Venice	4.2	-118.4859	33.9927	-118.4623	33.9631
Dockweiler	3.9	-118.4583	33.959	-118.4398	33.9284
ElSegundo	2.4	-118.4395	33.9275	-118.4291	33.9087
Manhattan	3.9	-118.4287	33.9078	-118.4127	33.8762
Hermosa	3.0	-118.4122	33.8754	-118.4027	33.8501
Redondo	3.0	-118.3929	33.8388	-118.3955	33.8123
Torrance	0.8	-118.3958	33.8114	-118.3983	33.8048

3.2.1. Experimental Design

The development of the lookup table, discussed in Section 2.3.1, enables us to write numerical codes, which loop through a time series of deep-water wave conditions; identify the closest modeled triplet of wave heights, periods, and directions; and extract the SWAN wave transformations for a selected bathymetry within the Southern California Bight. The heights, periods, and directions used in this experiment are three-hourly hindcasts for winter waves (December through March) of 1948–1998, at the deep-water site (33˚N, 122˚W) as provided by Graham and Diaz (2001) and analyzed by Adams et al. (2008). This time series of wave conditions was run through the SWAN-CGEM routines for the bathymetric nest "SntMnc," and longshore distributions of annual potential beach volume change were calculated for the 14 beaches identified in Table 3-2. These results were used in an economic model of beach use presented by Pendleton et al. (2008), for a complementary PIER study.

3.2.2. Results

Model results of the 50-year analyses of patterns of potential winter erosion/accretion along the Santa Monica Bay beaches are provided in Figures 3-6, 3-7, 3-8, 3-9, and 3-10. Annual rates of potential volumetric accretion were as high as ~800 cubic meters per meter (m^3/m) (Hermosa), and annual rates of potential volumetric erosion were as high as -2,500 m^3/m (Torrance). Most beaches exhibited regions of consistent accretion and regions of consistent erosion. In all cases, annual potential volumetric beach change was most severe during the El Niño winter of 1982–1983, shown as a green line in Figures 3-6 through 3-10.
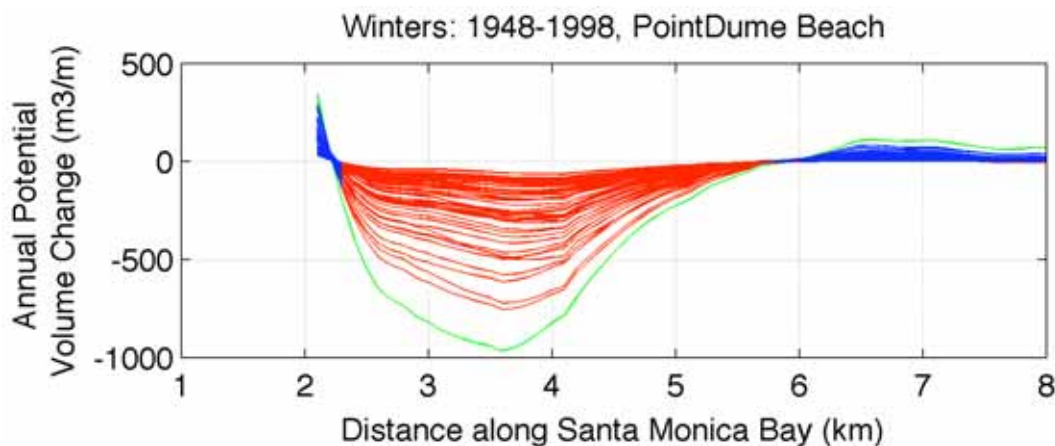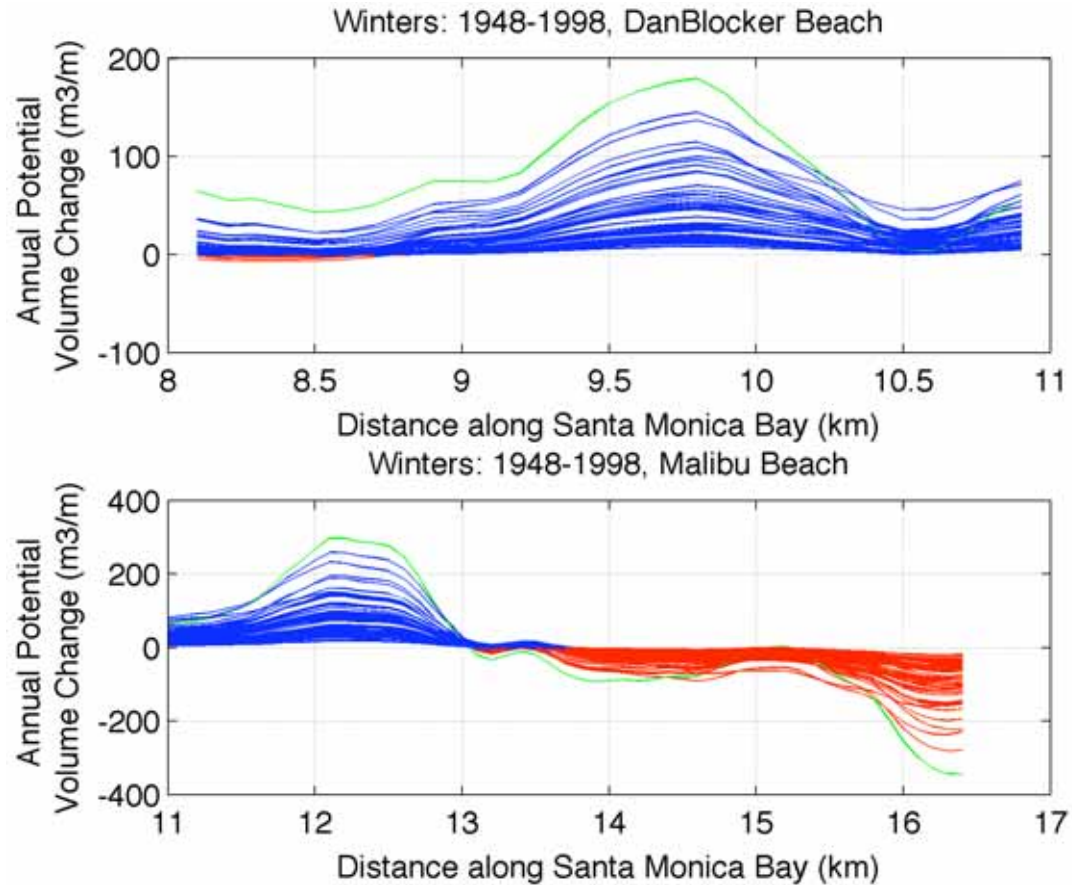
Figure 3-6. Divergence of drift analyses for 50-year period (winters of 1948–1998) for beaches Point Dume, DanBlocker, and Malibu. Each continuous line is one year's cumulative potential beach volume change. Blue portions show regions of accretion, red portions show regions of erosion. The El Niño winter of 1982–1983 is shown in green, for reference. Alongshore distance is measured in kilometers from Point Dume proper.
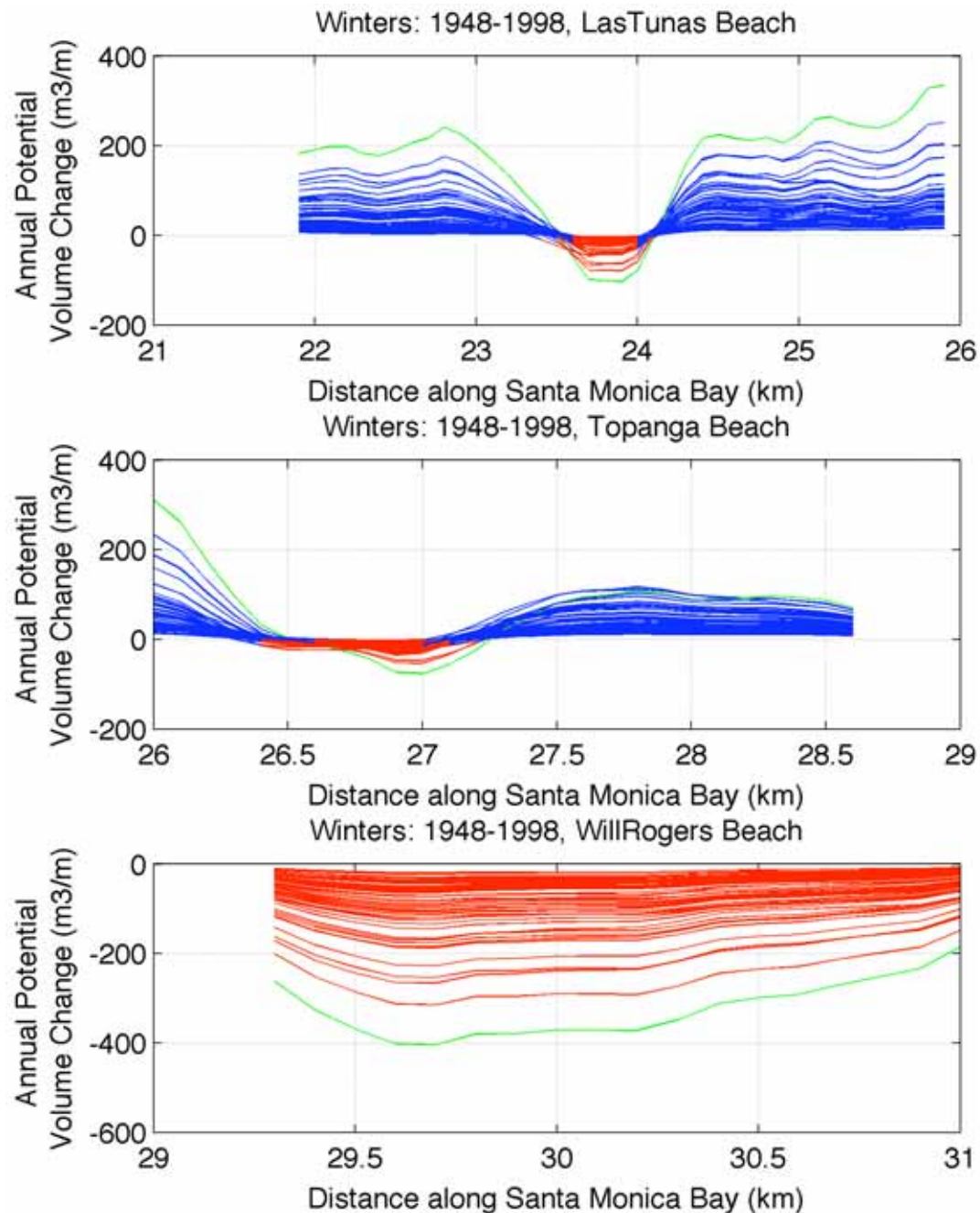
Figure 3-7. Divergence of drift analyses for a 50-year period (winters of 1948–1998) for beaches LasTunas, Topanga, and WillRogers. Each continuous line is one year's cumulative potential beach volume change. The blue portions show regions of accretion, and the red portions show regions of erosion. The El Niño winter of 1982–1983 is shown in green, for reference. Alongshore distance is measured in kilometers from Point Dume proper.

50
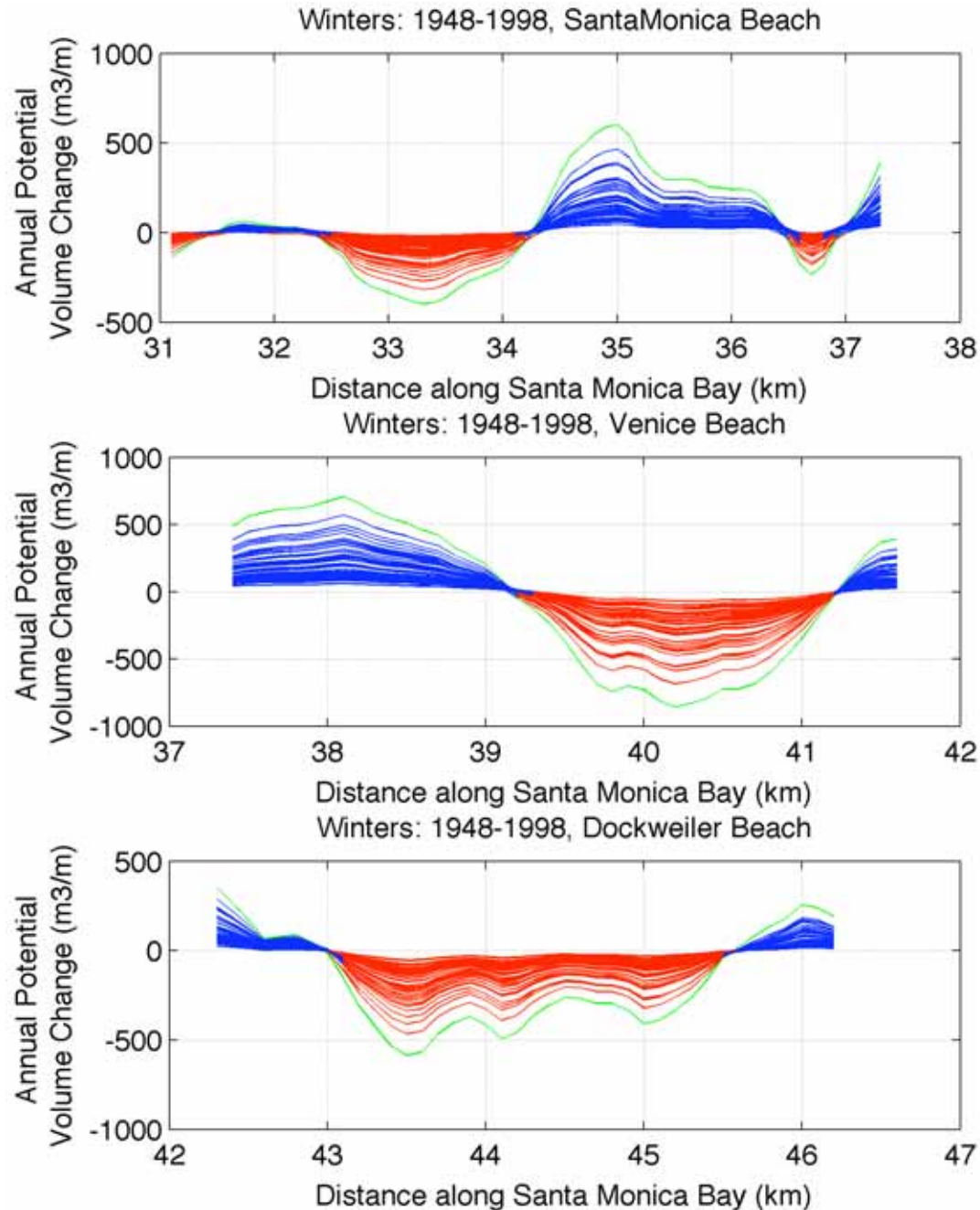
Figure 3-8. Divergence of drift analyses for a 50-year period (winters of 1948–1998) for beaches Santa Monica, Venice, and Dockweiler. Each continuous line is one year's cumulative potential beach volume change. The blue portions show regions of accretion, and the red portions show regions of erosion. The El Niño winter of 1982–1983 is shown in green, for reference. Alongshore distance is measured in kilometers from Point Dume proper.

51
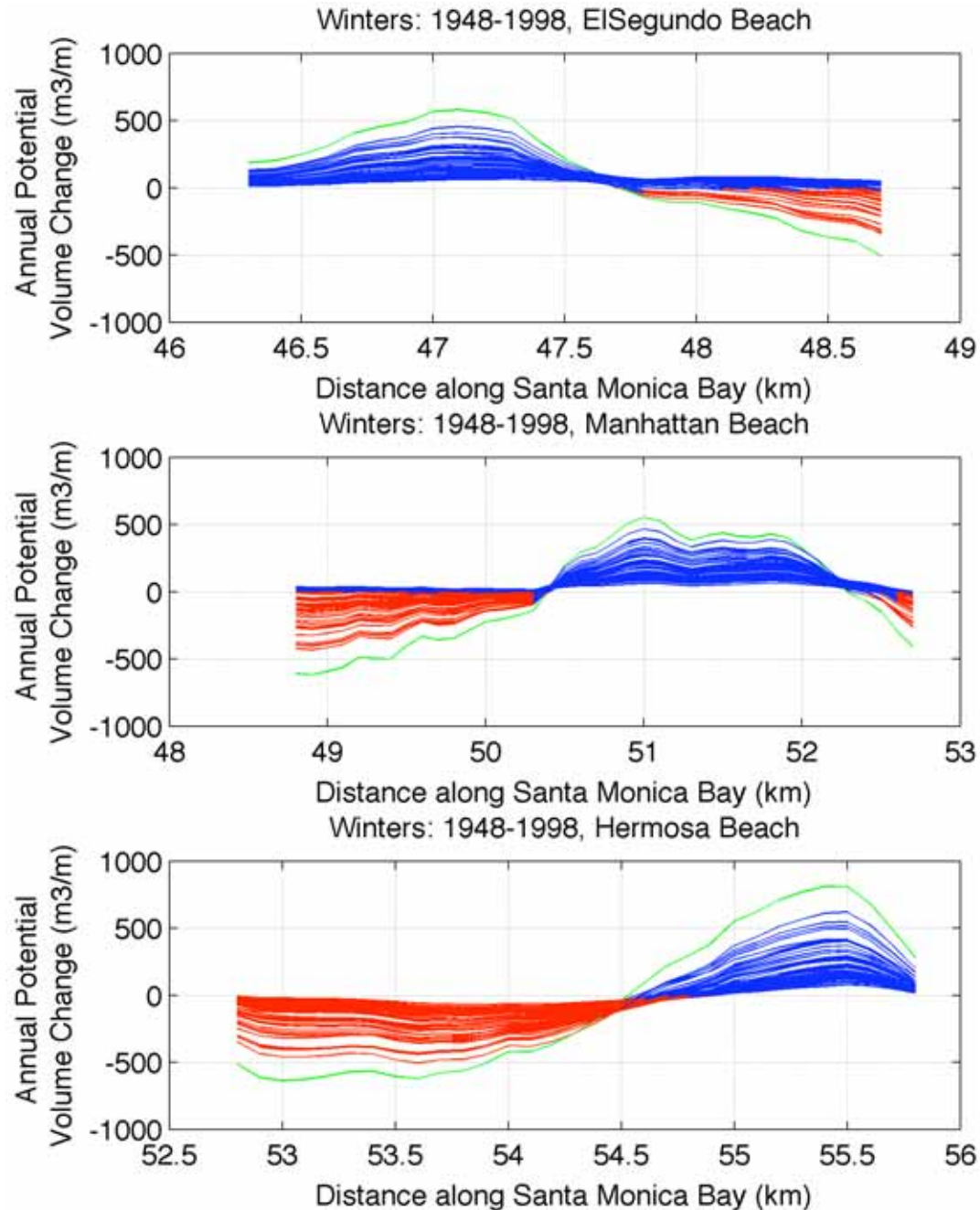
Figure 3-9. Divergence of drift analyses for a 50-year period (winters of 1948–1998) for beaches El Segundo, Manhattan, and Hermosa. Each continuous line is one year's cumulative potential beach volume change. The blue portions show regions of accretion, and the red portions show regions of erosion. The El Niño winter of 1982–1983 is shown in green, for reference. Alongshore distance is measured in kilometers from Point Dume proper.

52
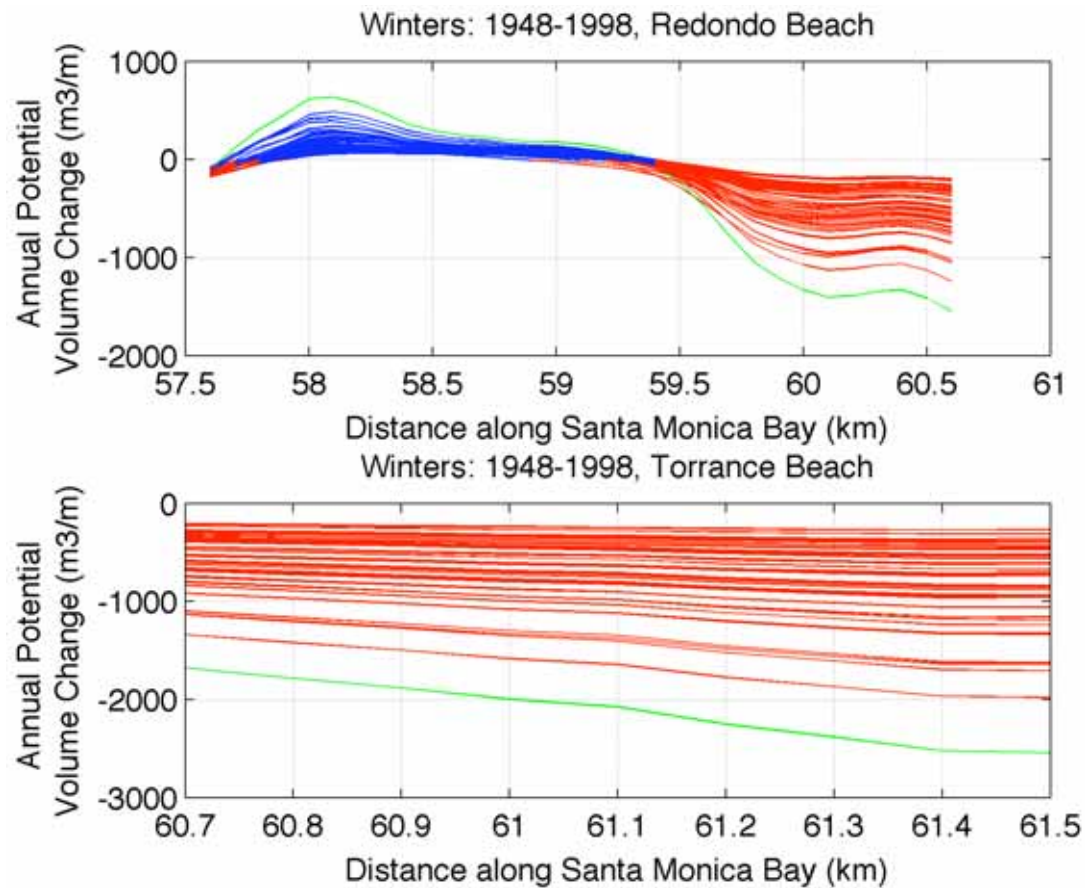
Figure 3-10. Divergence of drift analyses for a 50-year period (winters of 1948–1998) for beaches Redondo and Torrance. Each continuous line is one year's cumulative potential beach volume change. The blue portions show regions of accretion, and the red portions show regions of erosion. The El Niño winter of 1982–1983 is shown in green, for reference. Alongshore distance is measured in kilometers from Point Dume proper.

Figure 3-11 illustrates the daily divergence of drift calculated for one beach over the course of two winters: a strong La Niña winter (1973–1974) and a strong El Niño winter (1982–1983). The temporal pattern of divergence of drift during the strong El Niño winter reveals much more frequent large-scale erosional events in the erosional portion of the beach (between 54.5–56 km from Point Dume). It is notable, but perhaps purely coincidental, that the difference in timing of erosional events, when comparing the La Niña and El Niño winters, illustrates that the bulk of severe, damaging storms occur later in the winter season during El Niño winters.
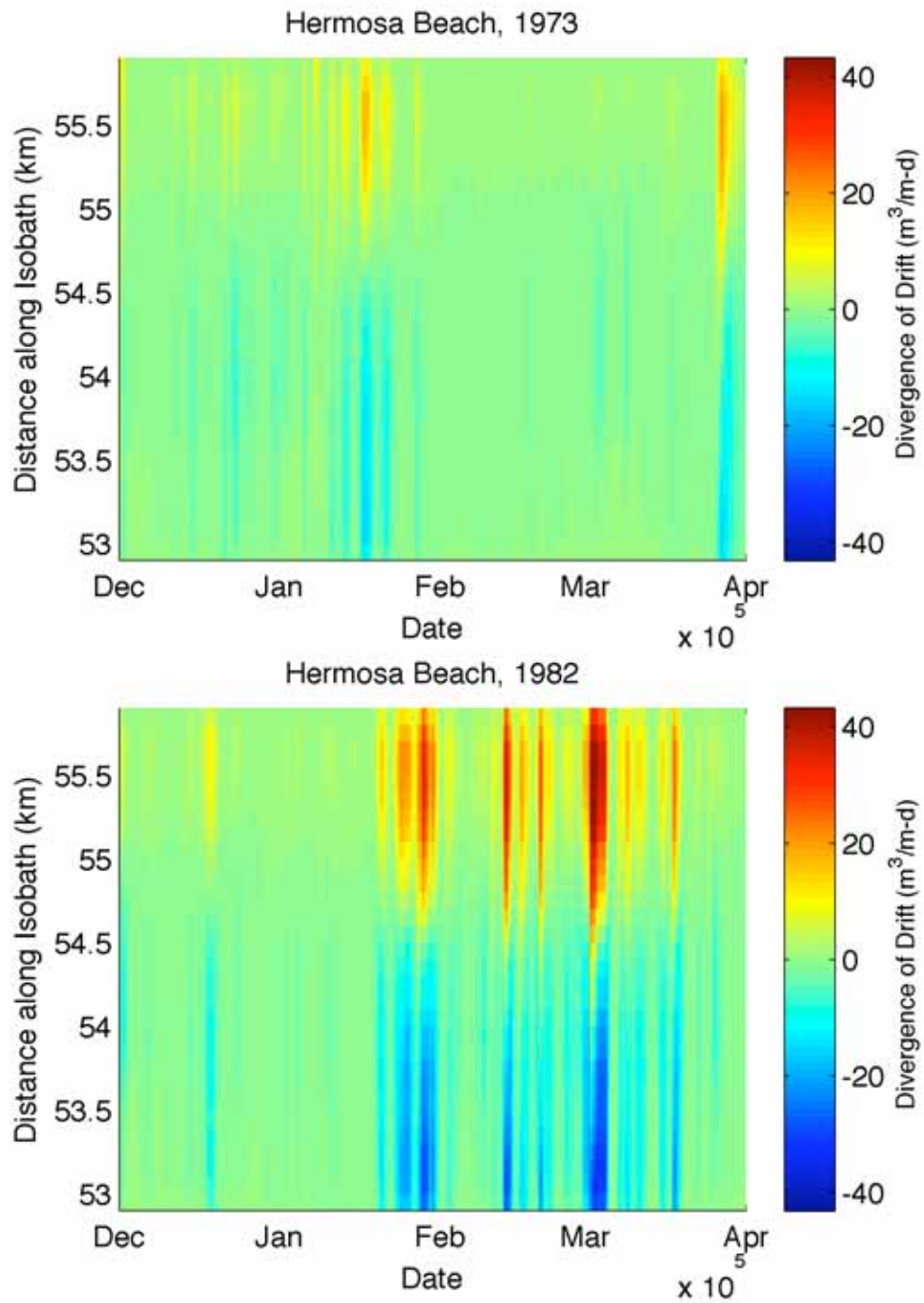
Figure 3-11. Comparison of divergence of drift for a strong La Niña winter (1973–1974) versus a strong El Niño winter (1982–1983) for Hermosa Beach within the "SntMnc" nest.

3.2.3. Experimental Conclusions and Implications

From the erosional hotspot likelihood experiments, the following conclusions can be drawn:

For the beaches of the "SntMnc" coastal nest, the following beaches are considered to be chronically erosional: PointDume, WillRogers, Dockweiler, and Torrance. Only two beaches, DanBlocker and LasTunas, are considered to be continuously accretional. And the remaining eight beaches (Malibu, Topanga, SantaMonica, Venice, ElSegundo, Manhattan, Hermosa, and Redondo) are mixed in their trend of sedimentary health, exhibiting both erosional and accretional reaches. A valuable check on the modeling performed during this experiment would be a comparison of these results with beach nourishment statistics for beaches of Los Angeles County.

In every beach examined, the 1982–1983 El Niño winter yielded the most dramatic potential beach volume changes, irrespective of whether those changes were erosional or accretional. This conclusion points to an important implication that highlights a consistent, recurring theme in geomorphology and Earth science; namely, that the "extreme," relatively infrequent, events dominate landscape change. This is not a new conclusion, as numerous studies have referenced the dramatic coastal changes witnessed during El Niño winters, but the experiments conducted during this project bolster the general consensus of the geomorphological community.

Lastly, it should be noted that numerous studies have shown that beaches "recover" after an erosional event (lasting one to several days) over a time period of days to weeks. Often, the accretionary pattern associated with a recovery appears as a mirror-image of the spatial pattern of erosion the beach experiences during the storm event (e.g., List et al. 2006). Though the causes and mechanics of the recovery are not well understood, this behavior implies that a dynamic equilibrium of beach morphology exists in tune with a characteristic wave climate for a coastal region.

3.3. Estimating Sea Cliff Retreat from Sea Level Rise

Sea level rise is one of the major concerns associated with climate change. In addition to the effects of flooding/coastal inundation, there is a concern that changing water levels effectively changes the nearshore bathymetry, which may have a significant effect on the distribution of coastal wave energy alongshore. Naturally, the coastal landscape will adjust to this new distribution of wave energy by seeking a new dynamic equilibrium; accomplished by eroding some portions of shoreline and accreting others. In this section, we explore the effect of a +1 meter rise in sea level on the natural position of sea cliff, along a well-studied, stable portion of the central coast of San Diego county between 32.8˚ and 33.15˚ N latitude, identified above as the "TorPns" coastal nest. This +1 meter rise in sea level is within the range predicted by some recent sea level rise studies for the next century, but is not based on an exact greenhouse gas emission scenario.

3.3.1. Background for Calculations

Sea level rise along coasts with sea cliffs and rock platforms always involves cliff erosion and a landward extension of the rock platform. In cases where sea cliff erosion rate cannot keep pace with sea level rise, as is often the case for cliff faces of plutonic rock,

lava flows and engineered cement walls, sea level may rise against a nearly vertical sea cliff, eventually resulting in a plunging cliff coast. However, coasts with sea cliffs and platforms of more easily eroded sedimentary material usually begin to erode and adjust to the rising sea level, as shown by the many studies of submerged and emerged terraces along the California coast. Depending on the dominant process responsible for sea cliff erosion, platform and sea cliff cutting proceed most effectively when a full, protective beach cover is not present. The absence of equilibrium beaches precludes the application of concepts such as the divergence of the drift and hot spot analysis. Modeling this situation requires the occasional activation of sea cliff and platform cutting modules, which is the next step in our modeling effort. However we do have a well-established understanding of the processes involved in terracing by wave action during sea level rise. This understanding leads to geometric relations that can be applied to cliff erosion and platform cutting that can be predicted from sea level rise as discussed in the following.

We select a section of coastline that is stable and has a known history of stability for millennia, such as the Torrey Pines block between La Jolla and Solana Beach in the Oceanside littoral cell. The Torrey Pines subcell from the head of Scripps Submarine Canyon to Solana Beach contains some of the most stable coastline in southern California, with a small uniform uplift rate of 1.3 mm/yr established over the past 1,525 ka by the elevation/age relationship of emergent marine terraces (Kennedy and Tan 2008). However, the stability ends abruptly along the Rose Canyon fault that passes through La Jolla to the south and extends offshore to the west (e.g., Hogarth et al. 2007).

3.3.2. *Estimates of the Effects of Sea Level Rise*

We select the Torrey Pines subcell to illustrate the procedure for calculating the potential effect of sea level rise on the sea cliff and platform, noting that the small land uplift rate of 0.13 mm/yr is negligible in comparison to the existing sea level rise of about 3 mm/yr and the present estimated rise of about 1.4 m by the end of the century. Also, the sea cliffs and platforms consist of Eocene sedimentary formations of differing resistances to erosion (Inman et al. 2005a).

Seismic studies of the bottom and subbottom profiles show that the continental shelf off the Torrey Pines block consists of terraces cut into mostly Tertiary sediments representing stillstands of the various past sea levels. These submerged terraces supplement the emerged terraces now observed on land. In many cases the sea cliffs of the emerged terraces are steeper, representing the cliff face slope when cut before recession. However those for the submerged terraces are less steep, representing passage of the rising sea level. In both cases, the platform slopes are gentle and reflect the original wave-cut platform. Although the rate of sea level rise may enter as a factor in the slope relation for platform slopes, the major factor appears to be the erodibility of the rock formation (e.g., Inman et al. 2005b; Sunamura 1992).

In the following discussion we define the platform as the sub-horizontal bedrock surface attached to, and extending seaward (X) from the existing sea cliff base. The platform slopes at angle β from the plane defined by present mean sea level (MSL). The relation is shown schematically in Figure 3-12 for present sea level, with a landward position to

accommodate future sea level rise (SLR') and sea cliff erosion (SCE'). The slope of the present platform is given by the relation

$$\tan\beta = h/X$$

while that for the future platform β' may be slightly smaller or greater,

$$\beta' \leq \beta \leq \beta'$$
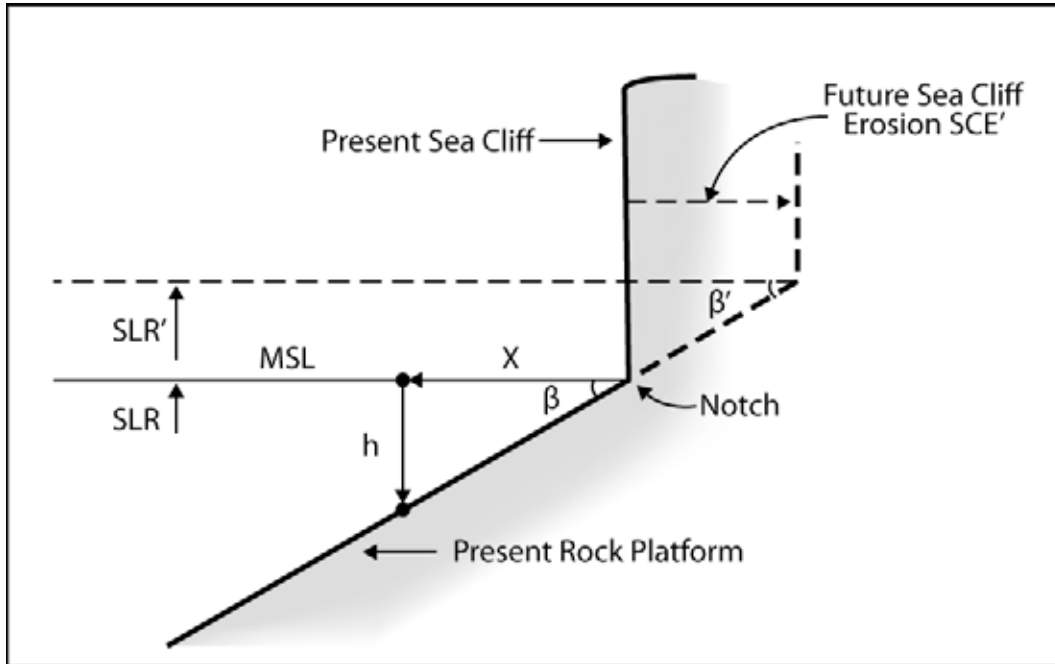
Figure 3-12. Schematic representation of the present wave-cut platform and eroding sea cliff which are assumed to be in equilibrium with present mean sea level (MSL) and the present slow rate of mean sea level rise (SLR), resulting in an angle β between MSL and the sloping platform surface tan β = h / X.

For purposes of comparison, we assume that the composition of the future sea cliff and platform remain the same as the present so that to a first approximation, β' is equal to β. Future wave forcing may increase as a result of climate change, while future rates of sea level rise will certainly increase. Since the slope of the platform is likely to decrease with increasing wave intensity and increase with increasing rate of sea level rise, the two effects may partially cancel each other.

Analysis of the platform slopes for the six seismic profiles of platforms measured along the Torrey Pines subcell show that the slopes β adjacent to the sea cliffs range from about 1.0% to 2.9%, with a median value of about 2.1%. A slope of 2.1% suggests that a sea level rise of 1 meter could result in a sea cliff retreat of about 47 m, while an estimated sea level rise of 1.4 m by 2100 AD will cause a cliff retreat of 67 m. The present sea cliff retreat rate of about 5 cm/yr (Young and Ashford 2006) would result in a retreat of 4.5 m by 2100 AD. This suggests we can expect coastal cliff erosion to increase by factors of 10 to 15 times the present rate.

4.0 References

Adams, P.N., Inman, D.L., and Graham, N.E. 2008. "Southern California deep-water wave climate: Characterization and application to coastal processes." *Journal of Coastal Research* 24: 1022–1035.

Anderson, R.S., Densmore, A.L., and Ellis, M.A. 1999. "The generation and degradation of marine terraces." *Basin Research* 11: 7–19.

Ashton, A., Murray, A.B., and Arnault, O. 2001. "Formation of coastline features by large-scale instabilities induced by high-angle waves." *Nature* 414: 296–300.

Bagnold, R.A. 1963. Beach and Nearshore Processes - Part 1, Mechanics of marine sedimentation, *in* Hill, M.N., ed., *The sea - ideas and observations on progress in the study of the sea,* Volume 3: New York and London, John Wiley and Sons, p. 507–528.

Bayram, A., Larson, M., and Hanson, H. 2007. "A new formula for the total longshore sediment transport rate." *Coastal Engineering* 54: 700–710.

Booij, N., Ris, R.C., and Holthuijsen, L.H. 1999. "A third-generation wave model for coastal regions - 1. Model description and validation." *Journal of Geophysical Research-Oceans* 104: 7649–7666.

Cayan, D.R., Bromirski, P.D., Hayhoe, K., Tyree, M., Dettinger, M.D., and Flick, R.E. 2008. "Climate change projections of sea level extremes along the California coast." *Climatic Change* 87: S57–S73.

Cayan, D.R., Redmond, K.T., and Riddle, L.G. 1999. "ENSO and hydrologic extremes in the western United States." *Journal of Climate* 12: 2881–2893.

Farnsworth, K.L., and Milliman, J.D. 2003. "Effects of climatic and anthropogenic change on small mountainous rivers: The Salinas River example." *Global and Planetary Change* 39: 53–64.

Flick, R.E., Murray, J.F., and Ewing, L.C. 2003. "Trends in United States tidal datum statistics and tide range." *Journal of Waterway Port Coastal and Ocean Engineering-ASCE* 129: 155–164.

Graham, N.E. 2003. Variability in the wave climate of the North Pacific: Links to inter-annual and inter-decadal variability. Oceans 2003 Conference: San Diego, Marine Technology Society, p. 969–972.

Graham, N.E., and Diaz, H.F. 2001. "Evidence for intensification of North Pacific winter cyclones since 1948." *Bulletin of the American Meteorological Society* 82: 1869–1893.

Griggs, G.B., Patsch, K.B., and Savoy, L.E. 2005. *Living with the Changing California Coast.* University of California Press. 540 pp.

Hancock, G.S., and Anderson, R.S. 2002. "Numerical modeling of fluvial strath-terrace formation in response to oscillating climate." *Geological Society of America Bulletin* 114: 1131–1142.

Hasselmann, K., Barnett, T.P., Bouws, E., Carlson, H., Cartwright, D.E., Enke, K., Ewing, J.A., Gienapp, H., Hasselmann, D.E., Kruseman, P., Meerburg, A., Mller, P., Olbers, D.J., Richter, K., Sell, W., and Walden, H. 1973. "Measurements of wind-wave growth and swell decay during the Joint North Sea Wave Project (JONSWAP)." *Ergnzungsheft zur Deutschen Hydrographischen Zeitschrift Reihe* 8: 95.

Hogarth, L.J., Babcock, J., Driscoll, N.W., Le Dantec, N., Haas, J.K., Inman, D.L., and Masters, P.M. 2007. "Long-term tectonic control on Holocene shelf sedimentation offshore La Jolla, California." *Geology* 35: 275–278.

Inman, D.L. 2005. Littoral Cells, *in* Schwartz, M., ed., *Encyclopedia of Coastal Science: Dordrecht,* Netherlands, Springer.

Inman, D.L., and Bagnold, R.A. 1963. Beach and Nearshore Processes - Part II. Littoral Processes, *in* Hill, M.N., ed., *The sea - ideas and observations on progress in the study of the sea,* Volume 3: New York and London, John Wiley and Sons. 529–553.

Inman, D.L., and Frautschy, J.D. 1965. Littoral Processes and the Development of Shorelines. Santa Barbara Specialty Conference on Coastal Engineering, A.S.C.E.

Inman, D.L., and Jenkins, S.A. 1999. Climate change and the episodicity of sediment flux of small California rivers. *Journal of Geology* 107: 251–270.

Inman, D.L., Masters, P.M., Adams, P.N., and Hogarth, L.J. 2005a. *Facing the Coastal Challenge: Past, Present, and Future Erosion and Position of the Southern California Coast* (Final Report). Kavli Institute.

Inman, D.L., Masters, P.M., and Jenkins, S.A. 2005b. Facing the Coastal Challenge: Modeling Coastal Erosion in Southern California, *in* Magoon, O.T., ed., *California and the World Ocean,* Reston, Virginia, A.S.C.E., p. 1431.

Inman, D.L., and Nordstrom, C.E. 1971. "Tectonic and Morphologic Classification of Coasts." *Journal of Geology* 79: 1–21.

Kalnay, E., Kanamitsu, M., Kistler, R., Collins, W., Deaven, D., Gandin, L., Iredell, M., Saha, S., White, G., Woollen, J., Zhu, Y., Chelliah, M., Ebisuzaki, W., Higgins, W., Janowiak, J., Mo, K.C., Ropelewski, C., Wang, J., Leetmaa, A., Reynolds, R., Jenne, R., and Joseph, D. 1996. "The NCEP/NCAR 40-year reanalysis project." *Bulletin of the American Meteorological Society* 77: 437–471.

Kaminsky, G.M., and Kraus, N.C. 1993. Evaluation of depth-limited wave breaking criteria, Proceedings of 2nd International Symposium on Ocean Wave Measurement and Analysis, Waves 93: New York, ASCE. 180–193.

Kamphuis, J.W. 1991. "Alongshore Sediment Transport Rate." *Journal of Waterway Port Coastal and Ocean Engineering-ASCE* 117: 624–640.

Kamphuis, J.W., Davies, M.H., Nairn, R.B., and Sayao, O.J. 1986. "Calculation of Littoral Sand Transport Rate." *Coastal Engineering* 10: 1–21.

Kennedy, M.P., and Tan, S.S. 2008. Geologic Map of the San Diego 30 x60 Quadrangle, California, California Department of Conservation, California Geological Survey, p. 21 pp., 2 plates.

Kistler, R., Kalnay, E., Collins, W., Saha, S., White, G., Woollen, J., Chelliah, M., Ebisuzaki, W., Kanamitsu, M., Kousky, V., van den Dool, H., Jenne, R., and Fiorino, M. 2001. "The NCEP-NCAR 50-year reanalysis: Monthly means CD-ROM and documentation." *Bulletin of the American Meteorological Society* 82: 247–267.

Komar, P.D. 1998. *Beach Processes and Sedimentation.* Prentice-Hall, Inc. 544 pp.

Komar, P.D., and Gaughan, M.K. 1972. Airy Wave Theory and Breaker Height Prediction, Proceedings of the 13th Coastal Engineering Conference, Amer. Soc. Civil Engrs. 405–418.

Komar, P.D., and Inman, D.L. 1970. "Longshore Sand Transport on Beaches." *Journal of Geophysical Research* 75: 5914–5927.

Larson, M., and Kraus, N.C. 1989. *SBEACH: Numerical model for simulating storm-induced beach change; Report 1, Empirical foundation and model development.* Vicksburg, Mississippi, U.S. Army Engineer Waterways Experiment Station, Coastal Engineering Research Center.

Legg, M.R. 1991. Developments in understanding the tectonic evolution of the California Continental Borderland, *in* Osborne, R.H., ed., *From Shoreline to Abyss: Contributions in Marine Geology in Honor of Francis Parker Shepard.* Tulsa, Okla., Society for Sedimentary Geology. 291–312.

List, J.H., Farris, A.S., and Sullivan, C. 2006. "Reversing storm hotspots on sandy beaches: Spatial and temporal characteristics." *Marine Geology* 226: 261–279.

List, J.H., Hanes, D.M., and Ruggiero, P. 2007. Predicting longshore gradients in longshore transport: Comparing the CERC formula to Delft3D, Proceed. 30th International Conference on Coastal Engineering: San Diego, California, World Scientific. 3370–3380.

Longuet-Higgins, M.S., and Stewart, R.W. 1964. Radiation stresses in water waves; a physical discussion, with applications: Deep-Sea Research, v. 11. 529–562.

MacGregor, K.R., Anderson, R.S., Anderson, S.P., and Waddington, E.D. 2000. "Numerical simulations of glacial-valley longitudinal profile evolution." *Geology* 28: 1031–1034.

Milliman, J.D. 1995. "Sediment discharge to the ocean from small mountainous rivers: The New Guinea example." *Geo-Marine Letters* 15: 127–133.

Milliman, J.D., and Syvitski, J.P.M. 1992. "Geomorphic Tectonic Control of Sediment Discharge to the Ocean — The Importance of Small Mountainous Rivers." *Journal of Geology* 100: 525–544.

O'Reilly, W.C. 1993. "The southern California wave climate: effects of islands and bathymetry." *Shore & Beach* 61: 14–19.

O'Reilly, W.C., and Guza, R.T. 1993. "A Comparison of 2 Spectral Wave Models in the Southern California Bight." *Coastal Engineering* 19: 263–282.

Pawka, S.S. 1983. "Island Shadows in Wave Directional Spectra." *Journal of Geophysical Research-Oceans and Atmospheres* 88: 2579–2591.

Pawka, S.S., Inman, D.L., and Guza, R.T. 1984. "Island Sheltering of Surface Gravity-Waves - Model and Experiment." *Continental Shelf Research* 3: 35–53.

Pelnard-Considere, R. 1956. Essai de theorie de l'evolution des forms de ravage en plage de sable et de galets: 4me Journees de l'Hydraulique, Les Energies de la Mer, v. Question III, p. 289–298.

Rogers, W.E., Kaihatu, J.M., Hsu, L., Jensen, R.E., Dykes, J.D., and Holland, K.T. 2007. "Forecasting and hindcasting waves with the SWAN model in the Southern California Bight." *Coastal Engineering* 54: 1–15.

Rosati, J.D., Walton, T.L., and Bodge, K. 2002. Longshore Sediment Transport, *in* King, D., ed., *Coastal Engineering Manual, Part III, Coastal Sediment Processes* Chapter 2-3, Volume Engineer Manual 1110-2-1100: Washington, D.C., U.S. Army Corps of Engineers.

Ruddiman, W.F. 2002. *Earth's climate: Past and future.* W. H. Freeman and Company.

Ruggiero, P., List, J., Hanes, D.M., and Eshleman, J. 2006. Probabilistic Shoreline Change Modeling, 30th International Conference on Coastal Engineering: San Diego, California. American Society of Civil Engineers.

Shepard, F.P., and Emery, K.O. 1941. Submarine Topography off the California Coast: Canyons and Tectonic Interpretation. Geological Society of America Special Paper No. 31, p. 171 pp.

Sunamura, T., 1992. *Geomorphology of Rocky Coasts.* Chichester, Wiley and Sons, 302 p.

Sverdrup, H.U., and Munk, W.H. 1947. *Wind, Sea, and Swell: Theory of Relations for Forecasting.* U.S. Navy Dept., Hydrographic Office, H.O. Pub. No. 601, p. 1–44.

Warrick, J.A., and Milliman, J.D. 2003. "Hyperpycnal sediment discharge from semiarid southern California rivers: Implications for coastal sediment budgets." *Geology* 31: 781–784.

White, T.E., and Inman, D.L. 1989. Measuring longshore transport with tracers, *in* Seymour, R.J., ed., *Nearshore Sediment Transport.* New York: Plenum. 287–312.

Young, A.P., and Ashford, S.A.. 2006. "Application of airborne LIDAR for seacliff volumetric change and beach-sediment budget contributions." *Journal of Coastal Research* 22: 307–318.